TECHNISCHE UNIVERSITÄT MÜNCHEN

NAT TUM School of Natural Sciences

Bachelor Thesis

Characterization of a Multi-Channel-THGEM detector for photon detection

Leonardo Bugia

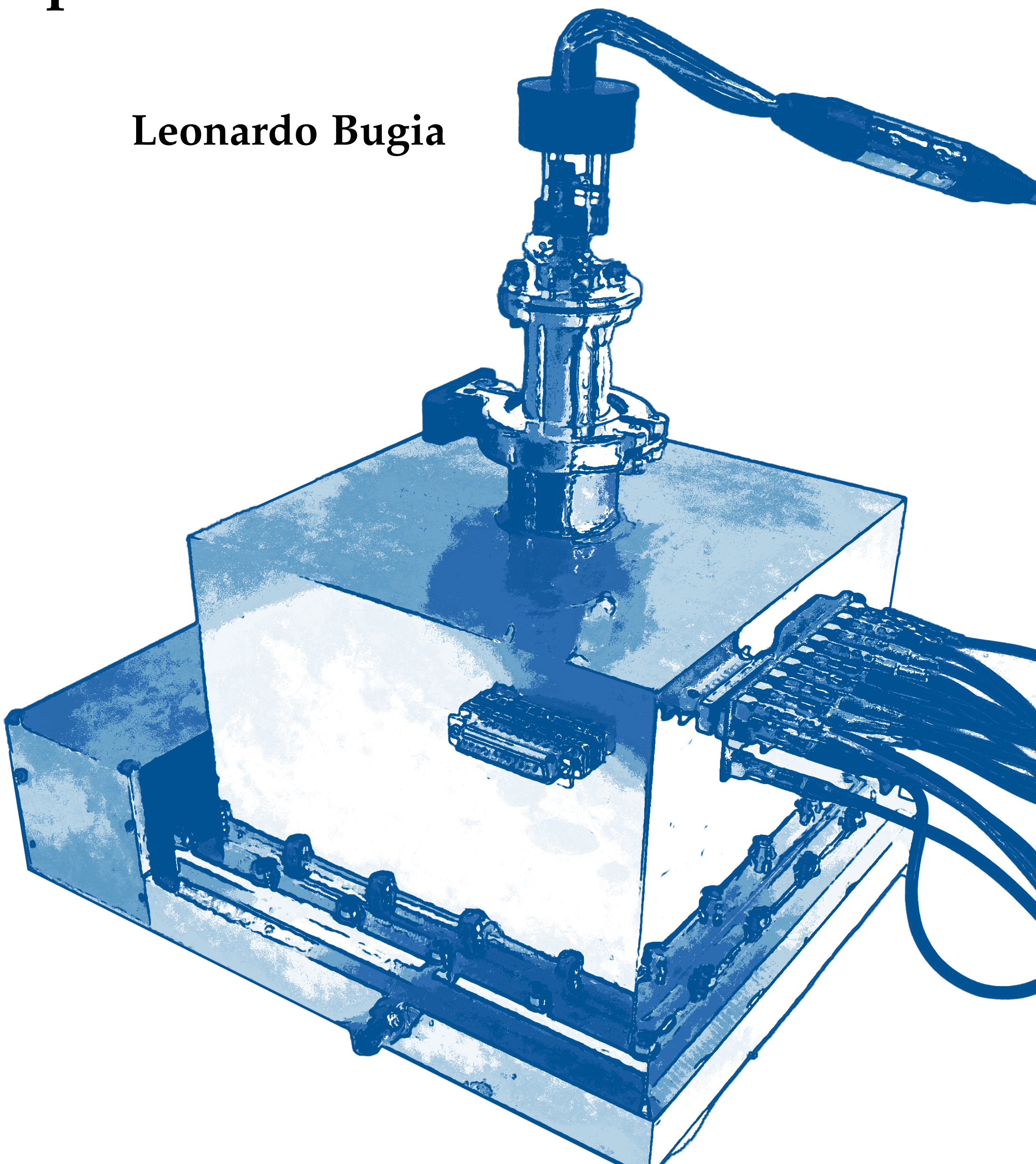

TECHNISCHE UNIVERSITÄT MÜNCHEN

TUM School of Natural Sciences

Characterization of a Multi-Channel-THGEM detector for photon detection

Charakterisierung eines Multi-Channel-THGEM-Detektors für den Nachweis von Photonen

Bachelor Thesis

Author: Leonardo Bugia
Examiner: Prof. Dr. Laura Fabbietti
Supervisor: Berkin Ulukutlu

Date: 16.10.2023

I confirm that the results presented in this bachelor's thesis is my own work and I have documented all sources and materials used.

Ich versichere, dass ich diese Bachelorarbeit selbstständig verfasst und nur die angegebenen Quellen und Hilfsmittel verwendet habe.

Munich, 16.10.2023 Leonardo Bugia

Abstract

Photon detection is one of the key measurement approaches utilized in many cutting-edge physics research. For this, detector technologies such as Photomultiplier tubes or Silicon Photomultipliers are most commonly used due to their great detection performance. However, for experiments aiming to measure in large areas, these technologies can be exceedingly costly. Here, Micro-Pattern-Gas-Detector based photon detectors promise to be a good alternative due to their ease of manufacturing at large scales. For this, over the years there have been many studies aiming to develop MPGD photodetectors, with an emphasis on investigating potential photocathode materials, especially for the detection of visible-range light. In this bachelor's thesis, a multi-pad THGEM-detector is tested for photon detection. The built detector contains two THGEMs, where the upper one is coated partially with a CsI reflective photocathode, and is extended by a newly designed multi-pad anode, which enables spatial granularity via measuring 64 individual pads. Initially, simulations of the electric field configurations of the detector are carried out accompanied by measurements to find optimal operating conditions. The focus is on maximizing the effective gain while keeping the ion bombardment to the photo-coating as low as possible, and the identified field configurations are used in the upcoming measurements. Furthermore, the detector is tested for photon detection using different light sources. First, a deuterium lamp is used to show that it is possible to measure the effect of the photo-coating on the individual pads for a continuous light beam. A clear impact of the photo-coating is observed. Finally, to demonstrate measuring short photon pulses a discharging THGEM (THGEM-lamp) is utilized as the light source. Although it is not possible to directly identify the signal from the photon pulses and disentangle it from the dominating discharge signal, a clear influence of the coating on the total signal amplitude is observed.

Contents

1 Introduction

1.1 Gaseous detectors operating principles

One of the most commonly employed family of devices for detecting and measuring charged particles is gaseous particle detectors. They work on the principle that charged particles passing through the gas will lead to the ionization of the gas molecules. An electric field is applied across the gas volume between two electrodes which prevents the recombination of the created electron ion pairs. The primary electrons created by these ionizations are then accelerated in the electric field towards the readout electrode, where a current proportional to the number of electrons is induced and can be measured by the readout electronics [1]. As charged particles pass through matter, they can interact with the particles of the matter. They can lose energy by inelastic scattering with the atoms of the material, which could lead to ionization and excitation. The energy loss can be measured by the resulting electrons and described by the Bethe Bloch formula [2]. This can be used to determine the type of the particle, provided its momentum is known. If the electric field is strong enough, the primary electrons can gain enough momentum that when they collide with other gas atoms, they can lead to additional ionizations. Thus, more electrons are produced which are also accelerated and so on. This process is called an avalanche and can be used to amplify the signal to make the measurement of the energy loss from single charged particles possible. A limiting factor to the operation of gaseous detectors in the proportional regime is the occurrence of discharges. When the electric field exceeds a certain threshold known as the Paschen limit [3] too many electron-ion pairs are created which can lead to the development of a discharge between two electrodes. This leads to a sudden increase of current, which results in a drop of the applied amplification field. Discharges should also be avoided as they can damage the fragile electrodes and readout electronics used in detectors. As gaseous detectors are among the oldest particle measurement technologies, many advancements have been made to improve their performance. One major leap was the introduction of Micropattern Gaseous Detectors (MPGDs). Thanks to advancements in micro-scale production technologies MPGDs employ structures that can constrain the area of amplification in a tiny region, with typical thickness in the sub-milimeter range. Gas Electron Multipliers (GEMs), which were first introduced by Sauli in [4], are one of the leading MPGD structures which have been used in many high-energy physics experiments like ALICE [5], COMPASS [6], ATLAS [7].

A GEM consists of a polyimide foil coated on both sides with thin copper foils and is etched to form small holes. A typical GEM is 50 µm thick and has holes with a pitch of 140 µm and a diameter of 70 µm [8]. Between the two sides of the GEM foil, a voltage is applied resulting in a high electric field in the holes. A similar type of detector is the Thick GEM (THGEM) [9, 10, 11], which is an approximately 10 times thicker version of a GEM with similar hole design. THGEMs are easier to produce and are more robust due to the scale of the structures, and offer a cheaper alternative to GEMs with slightly worse performance suitable especially for large-scale applications.

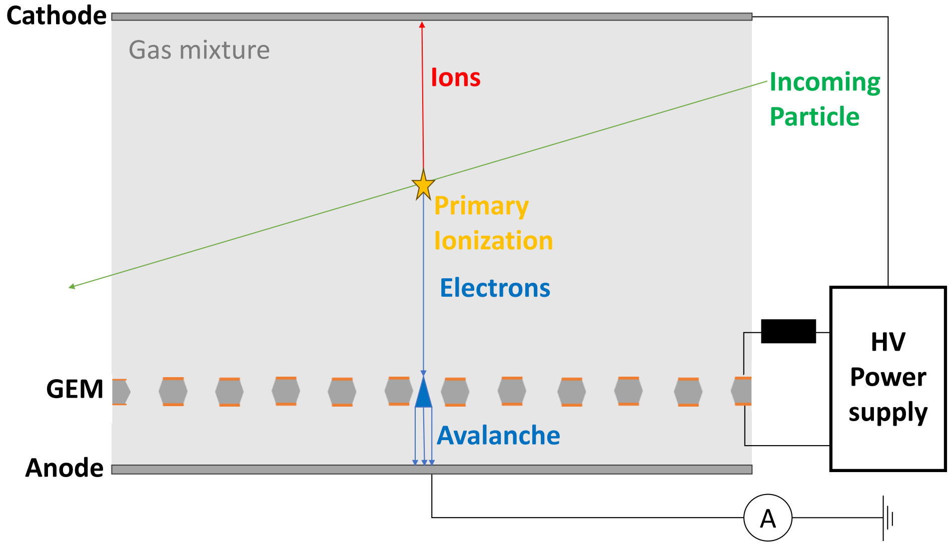

Figure 1.1: Working principle of GEM/THGEM detectors

The basic structure of a GEM-/THGEM-based detector is shown in figure 1.1. The detector is separated into three areas: The drift gap, the GEM, and the induction gap. The drift gap is the volume between the cathode and the top GEM foil in which the primary ionization happens. The primary electrons drift in a moderate electric field towards the GEM and are sucked into the GEM holes, where a high field is applied leading to the avalanche multiplication. The amplified electrons exit the GEM hole and move into the induction gap where a moderate field leads them to the readout anode connected to the readout electronics. The anode typically consists of small strips or pads, that can be read out individually to achieve some spatial resolution. A unique feature of GEMs/THGEMs is the possibility to use multiple GEMs/THGEMs in succession, which allows the electrons to be multiplied further. In this way, high amplification can be reached while keeping the individual fields below the Paschen limit and thus preventing discharges. For applications where high avalanche amplification is necessary using multiple layers is a great way to achieve this. Setups with up to 5 layers have been successfully utilized [12]. Another important component of gaseous detectors next to the amplification system is the gas used. The gas is typically composed of a mixture of counting and quenching gases. Counting gases form the main part of the gas and should have a high ionization probability to create and amplify electrons. Noble gases like Argon or Neon are particularly well suited for this purpose because of their electron configuration and on top of that do not interact that much with other particles. A side effect of using noble gases is that the ionized atom may be in an excited state and emit photons during deexcitation, which can lead to additional avalanches and finally the formation of discharges. Therefore, the quenching gas is introduced. The quenching gas typically consists of polyatomic gases like CH_4 or CO_2, which can absorb the photons and convert their energy into vibrations inside the molecule.

1.2 Photon detection with THGEM detectors

As described above, gaseous detectors rely on the ionization of gas molecules for the detection of incident particles such as charged particles of high-energy photons (X-rays). For the detection of photons that don't have enough energy to ionize gas atoms, a different method is needed to convert these photons into electrons. One successful approach has been to combine photo-sensitive materials with the cathode electrodes (so-called photocathodes). For this, one makes use of the photo effect, first postulated by Einstein in [13]. It describes the process of a photon hitting material, where an electron is released from the bond of an atom by absorbing a photon. Thereby, the energy of the photon must be as least as large as the binding energy of the electron. Excessive energy is converted into the kinetic energy of the emitted electron, which can be calculated by the equation:

$$E_{kin} = h \cdot f - W, \tag{1.1}$$

where W is the work function, which describes the energy needed to release an electron, and $E = h \cdot f$ is the energy of the photon, which is proportional to the frequency f of the light source. However, not every photon above this threshold leads to this effect. The probability for a photon to cause an electron emission is described as the quantum efficiency $\eta(\lambda)$ [14], which is dependent on the wavelength of the photon as well as the target material. Different materials have different spectra describing for which wavelength they are most sensitive. CsI is a photo-sensitive material that has a high quantum efficiency in the UV range, making it a good tool for measuring UV photons. To use THGEMs for photon detection one must combine them with photocathodes (PC) [15]. There are two methods of doing this. The first method is using a semitransparent PC on the entrance window of the detector. Alternatively, the other method uses a reflective PC coating on top of the THGEM electrode. In both cases, the drift field guides the electrons toward the THGEM holes, where they are amplified. As single photons produce a rather small signal high multiplication is needed, which can be assured by using multiple THGEMs. Prototypes with multiple THGEM layers and reflective coating have been tested in [16] for single photon detection.

One field of application lies in Cherenkov Ring Imaging (RICH). RICH detectors operate by measuring Cherenkov light emitted by particles in a transparent medium. When a charged particle passes through a medium at a speed greater than the phase velocity of light in that medium, Cherenkov light is emitted in a cone shape, whose aperture angle depends on the velocity of the particle. This cone is detected on a planar position-sensitive photon detector, where a ring-shaped pattern appears. By analyzing the ring shape one can determine the aperture angle of the cone and thus the velocity of the particle. If the momentum of the particle is known, for example through independent measurements prior to the RICH detector, one can calculate the mass of the particle and use it to identify the particle. There are various experiments, where THGEMs with photosensitive coatings have been employed in RICH detectors such as the COMPASS RICH-1 [17].

A key advantage of using coated THGEMs for photon detection compared to other photodetectors such as Photomultiplier tubes (PMTs) or Silicon Photomultipliers (SiPMs) is that they can be produced cost-effectively for large areas [18]. This would make photo-THGEM detectors a good alternative in applications such as neutrino observatories, where very large detection areas are needed if it can be shown that they can perform at a similar level in measuring visible photons.

2 Experimental setup and procedure

2.1 Experimental setup

The work conducted in the course of this thesis can be divided into three series of studies. Each measurement campaign was carried out using the same detector chamber that was built for the studies. The readout system and the sources were modified depending on the goals of each study. For the first measurement, the goal was to establish a good understanding of a double THGEM setup. Therefore, a ^{55}Fe source was used together with normal THGEMs and a single-pad anode. Additionally, simulations with Garfield++ and COMSOL were done in order to find the optimal operating conditions of the built detector. In the second measurement series a deuterium lamp was used as a continuous photon source and was combined with a CsI reflective photo-coating on areas on top of the first THGEM as well as a multi-pad readout electrode. The third measurement series aimed to demonstrate the measurement of short light-pulses with the constructed detector. As a photon source a discharge lamp composed of a single-hole-THGEM was used, while the readout remained the same as for the deuterium lamp measurements.

2.1.1 Detector

The built detector is composed of a wire plane acting as the drift cathode, a stack of two THGEMs, and an anode. The distances of the transfer- and induction-gap were set to 2 mm, whilst the drift-gap amounts to 3.6 mm. The THGEMs used consisted of a 400 µm thick PCB and a 35 µm thick copper electrode with a gold finish on each side. The hole pitch and diameter were 800 µm and 400 µm respectively. On both THGEMs a resistor is connected to the top electrode for better stability and to limit the rate of discharges. For photon detection measurements the first THGEM was partially coated with CsI-photo-sensitive material at TUM as shown in figure 2.1. Above the wires, the different sources are placed facing towards the THGEM stack. A gas-tight aluminum housing is used as the gas chamber. The chamber is constantly flushed by a gas mixture of

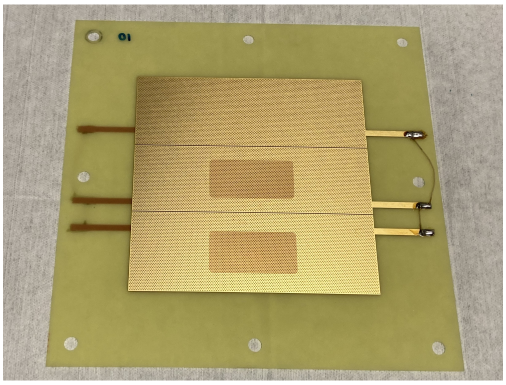

Figure 2.1: A picture of the partially CsI coated THGEM used in the photon detection measurements

Ar-CO_2 (90-10). All electrodes were connected to a high-voltage power supply.

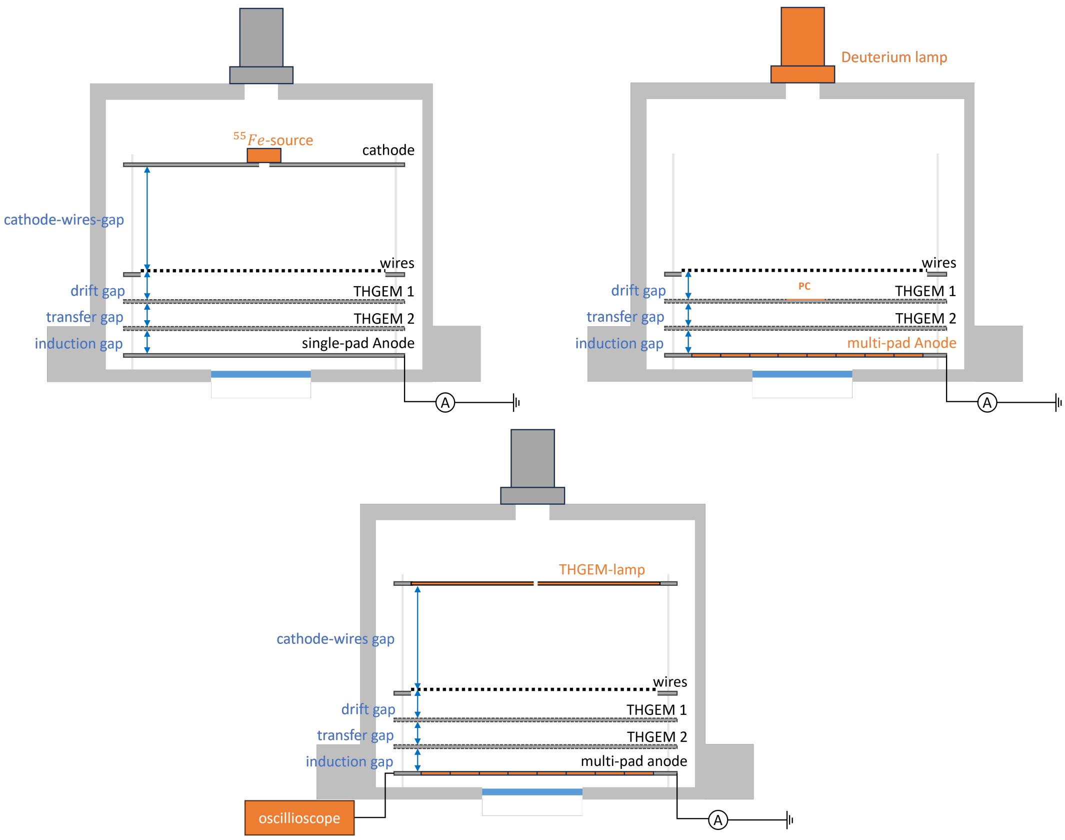

Figure 2.2: A sketch of the 3 different Setups, the important parts of each setup are highlighted in orange

Figure 2.2 (a) shows the sketch of the first setup used. An ^{55}Fe source was mounted on top of a cathode 30 mm above the wires. The cathode, which has a hole in the center acting also as a collimator, was used for positioning the source. The cathode extends the structure by another drift gap named the cathode-wires gap. As it is located above the basic structure of the detector and in further measurements the primary electrons are created on top of the first THGEM the additional field doesn't change any functionality of the detector and just serves as a support for the iron-source measurements. As the anode, a single-pad anode was used. The different electrodes were connected to a picoAmmeter (pAmmeter) produced by PicoLogic [19] before going to the High Voltage power supply and the different currents were measured.
For the second measurement series, the cathode and iron source were removed and replaced by the deuterium lamp mounted on top of the lid outside the chamber. The lamp is located on top of a hole located at the center of the lid. The measurements were done using a partially coated THGEM as well as a normal uncoated THGEM as a reference. The anode was changed to the newly designed multi-pad anode and connected to the pAmmeter with the readout system explained in section 2.1.3. A sketch of the second setup can be seen in figure 2.2 (b).
In the third measurement series a single-hole tungsten THGEM (designated as THGEM-

lamp) was attached 30 mm above the wires. Voltages beyond the discharge limit were applied across the THGEM-lamp, this leads to the formation of sparks with a constant rate dictated by the RC behavior of the HV circuitry. A 500 MΩ resistor was connected to the bottom of the THGEM-lamp to turn down the discharge rate. Here, the multi-pad anode was used and the different pads were read out with an oscilloscope and the pAmmeter. The sketch for this setup is shown in figure 2.2 (c).

2.1.2 Sources

In this section, the different sources used will be explained as well as why these sources have been chosen.
The used ^{55}Fe source isotope, which decays by capturing electrons into ^{55}Mn, emits mostly K-alpha-1 X-rays with an energy of 5.9 keV. Because of its high rate, it was chosen for the measurements accompanying the simulations.
The deuterium lamp is a gas-discharge light source that emits a continuous light beam. It has a high intensity in the VUV-region and was used in this thesis to create a mapping of the coated regions of the THGEM using the multi-pad-readout system.
For the last measurement series aiming to measure light pulses, the initial designs involved pulsed LED. However, due to the fact that LEDs are incapable of producing light in the VUV spectrum, to which the CsI photo coating is sensitive, a different approach had to be taken. It has been shown that during discharges photons in the VUV-spectrum are created [20]. Therefore a single-hole THGEM was used to create the light pulse. The single hole THGEM was chosen so that the source of the discharge and emitted light can be located and thus local fluctuations in the signal can be prevented. Due to the increased robustness to high temperatures, a tungsten single-hole THGEM, which was already available at TUM, was used to make the light source less prone to damage from the many discharges sustained during operation.

2.1.3 Readout system

In order to achieve spatial resolution a multi-pad anode was required. This allows the measurement of the signal at different positions, by reading out the individual pads. For the first measurements, an old multi-pad anode was used. A picture of it can be seen in figure 2.3 (a). The old anode design consisted of a plane of 10 x 10 cm^2, which was separated into 32 pads and a combined border around it but wasn't ideal in design for the conducted studies. Firstly, the pads were rather large in comparison to the coated area, leading to no pad completely being covered by the coating as can be seen in the projection of the coated area onto the readout plane in figure 2.3 (b). Using smaller pads, which are completely covered by the coating, makes it possible to investigate the influence of the coating directly without complicated geometrical considerations. Another problem that is not directly related to the design is to read out the different pads they had to be connected directly to the connectors inside the chamber. With the limited amount of connectors available only up to 5 Pads could be read out at a time and to change to different pads one had to open the chamber and solder the connectors to the other pads. Every time after changing to different pads the chamber had to be fully flushed with gas, which can take several hours, and a full measurement of all pads would thus take multiple days. In order to improve the time and performance of the detector a new anode was designed and assembled with new connectors.

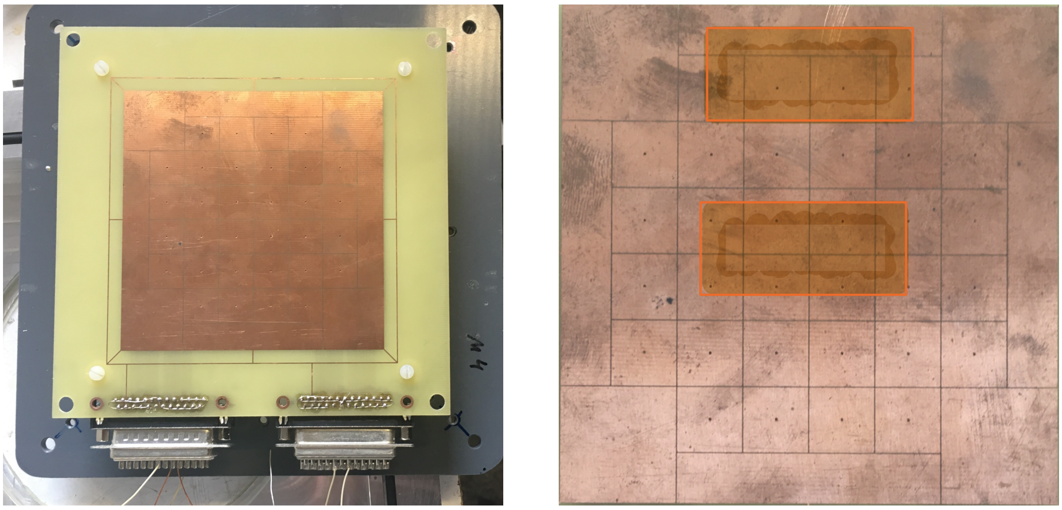

Figure 2.3: A picture of (a) the old Multi-Pad-Anode installed in the detector and (b) a projection of the coated area onto the readout plane

The new multi-pad anode was designed with Autodesk Fusion. The new design results from improvements to the shortcomings of the previously used one. Some design choices were taken so that it would also be compatible with another measurement setup at TUM (designated as Thomas Setup), which was used in the following studies [21] [22]. Firstly, the overall size was increased to match the size of the THGEMs. Therefore, it based on a 18 x 18 cm^2 PCB board with an electrode size of 11.2 x 11.2 cm^2. It is separated into 64 individual pads and a combined border around these. The pads are quadratic with a side length of 8.75 mm and the gap between two pads is 0.25 mm. Due to errors in production, the pads on the edge were missing. As a corrective measure, they were replaced with copper tape to minimize any significant change in the electric field. As it's not a perfect replacement some issues were expected on the outer fields. The individual pads were connected to four Sub-D-25 connectors on the bottom of the anode. The design with all four connectors on one side was chosen so it could be used in Thomas Setup. The smaller pads lead to better spatial resolution and if one takes a look at the projection of the coating onto the readout plane figure 2.5 (b) one can see that there are pads completely covered by the coating as well as some partially covered.

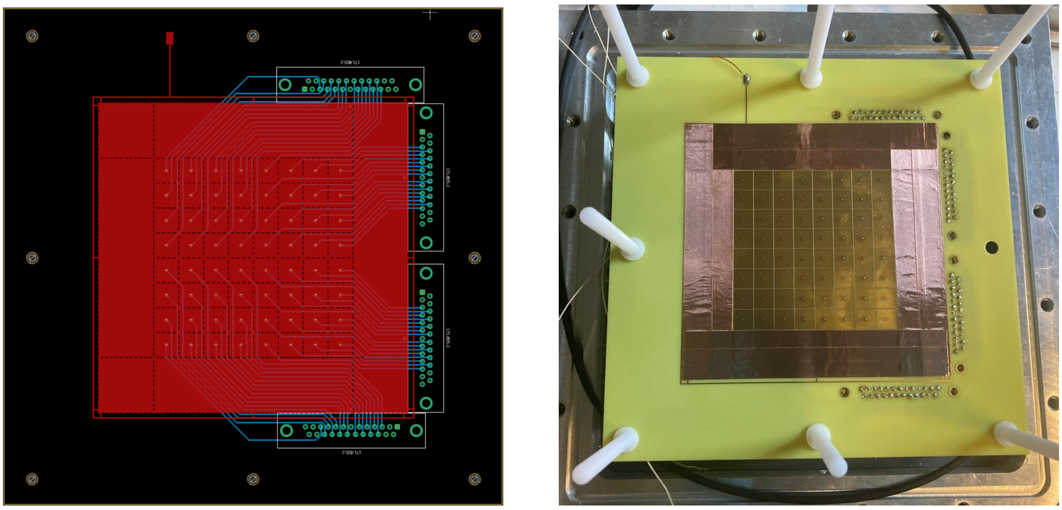

Figure 2.4: (a) The design of the new Multi-Pad-Anode in Autodesk and (b) a picture of the new Multi-Pad-Anode installed in the detector.

For better identification, a mapping of the pads was made and is shown in figure in 2.5 (a) The pads were classified into the sectors A, B, C, and D depending on the connector and were enumerated by the position in the connector.

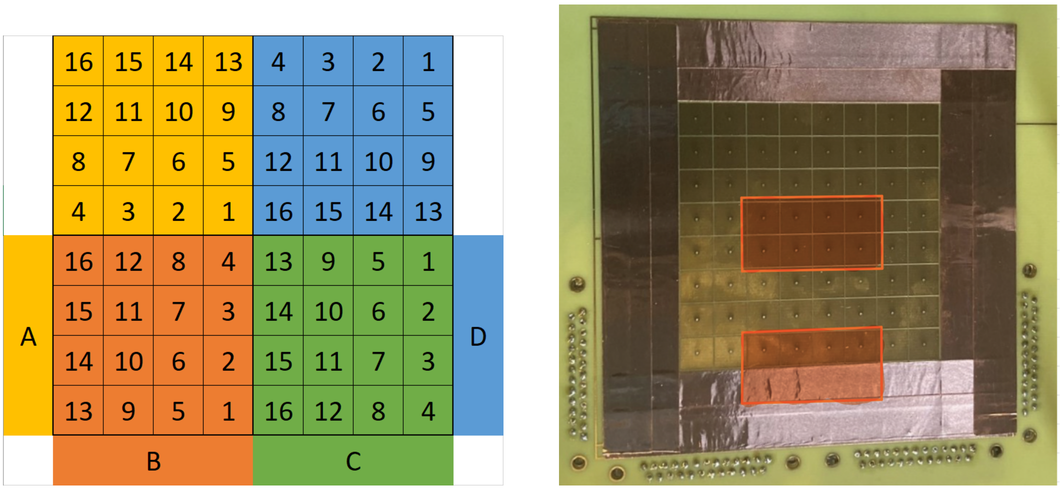

Figure 2.5: (a) Mapping of the multi-pad anode, different colors mark the different sectors (A, B, C, D) and (b) projection of the photo coating onto the readout plane of the new anode

To measure the individual pads without opening the chamber four cable assemblies were built. One end of these cables was attached to a gas-tight Sub-D-25 feed-through connector, which was embedded into the lid of the chamber. The other runs along the inner lid walls down to the anode where it can be connected for the measurements. The positioning of the cables was not optimal as one had to keep the detector halfway open to connect the cables to the anode, but because of the lack of space inside it was the best solution possible. The single pads can then be accessed individually with

an adaptor outside the chamber and connected to the readout system separately. To enable the grounding of the currently not measured pads three additional adaptors were made connecting those pads together to the ground. With this setup, all 64 pads could be accessed individually from outside the chamber while assuring that the rest is grounded.
During the discharge-lamp measurements aluminium foil was wrapped around the cables to act as shielding from the discharges to ensure the measured signal was caused by the signal on the pads and not by the signal reaching the cables.

2.2 Measurement methods

2.2.1 Gain

When looking at detector performance, a crucial quantity is the gain. It describes how well the avalanche multiplication process happens and is defined by the ratio of the number of amplified electrons to the number of primary electrons. However, the amplified electrons leaving the lower THGEM do not all reach the anode, as some of them are collected by the lowest THGEM-electrode. Therefore, we will distinguish between absolute and effective gain. The absolute gain takes the total number of amplified electrons into account, while the effective gain only considers the amplified electrons reaching the anode. The electrons reaching an electrode induce a signal proportional to their number. Therefore it is possible to calculate the effective gain by taking the ratio of currents:

$$G_{eff} = \frac{I_{anode}}{I_{prime}}, \tag{2.1}$$

where I_{Anode} refers to the current measured at the anode and I_{prime} refers to the primary current. The primary current can be measured by only applying the drift field and setting all other fields to zero. Therefore no avalanche can occur and all primary electrons are collected at the THGEM1 top inducing the primary current.

2.2.2 Ion bombardment

The Ion Back Flow (IBF) is defined as the ratio of ions reaching the cathode and electrons reaching the anode and can be calculated by the equation 2.2 with the measured currents of the anode and cathode.

$$IBF = \frac{I_{cathode}}{I_{anode}} \tag{2.2}$$

It is a quantity of how many ions float back into the drift gap towards the cathode. The rise of positively charged ions in the drift gap can influence the electric field and therefore impact the detector performance negatively. So the general attempt is to keep this factor as low as possible. A way to accomplish that is by using multiple GEMs/THGEMs which collect the ions created in avalanches and stop them from

reaching the drift gap.
Due to its fragile nature, the photo-coating on the first THGEM can be damaged if a large portion of ions "bombards" the top of the first THGEM. The consequences of the ion bombardment were studied in [21], where was shown that the ion bombardment has a negative influence on the quantum efficiency of the coating. We define the ion bombardment of THGEM1top (IB_{1top}) similar to IB by the ratio of ions reaching the top of THGEM1 and electrons at the anode.

$$IB_{1top} = \frac{I_{THGEM1top}}{I_{Anode}} \tag{2.3}$$

Since it can happen that avalanche electrons do not reach the anode due to, for example, the absence of an induction field, IB_{1top} greater than 1 is possible. However, under normal conditions, this should be smaller than 1.

2.2.3 Light measurements

The deuterium lamp measurements series were performed with the fields seen in table 2.1 and consisted of one measurement each with a coated and an uncoated THGEM. For both, the voltages were applied first and the lamp was switched on after a sufficient time, letting the THGEMs charge up before starting measurements. Since the lamp also needs a while to heat up, the measurement started after another 30 min It turned out that the intensity of the lamp still changes over time after heating up so one pad was connected to the pAmmeter during the whole measurement as a reference. For this pad C13 was chosen as it lies under the middle coating and therefore expects high currents, which makes the monitoring of the lamp behavior less prone to uncorrelated electronic fluctuations. With the other three channels of the pAmmeter three pads could be measured at a time. One measurement lasted around 100 seconds. Longer measurements weren't considered necessary as the statistical error was more than 3 orders of magnitude smaller. To allow comparison between individual pads, the measured currents were normalized by multiplying them with the ratio of the reference current of the first and its respective measurement.

Field name	electric field / voltage
$E_{Cat-Wires}$ [V/cm]	-
E_{Drift} [V/cm]	400
ΔV_{THGEM1} [V]	1000
E_{Trans} [V/cm]	2000
ΔV_{THGEM2} [V]	800
E_{Ind} [V/cm]	2000

Table 2.1: Electric fields/Voltages used in the measurement with the deuterium lamp

2.3 Discharge signal

Discharges are complicated phenomena that have been studied a lot in the last decades. Still, many details are not fully understood. Many factors have to be considered when looking at the signal. During a discharge an electromagnetic pulse is created which induces a signal into all electrodes it passes through. It can also lead to excitation or ionization of atoms in the gas. Thereby, electrons and ions are created, which can enter the amplification system and add up to the signal.

A typical signal shape of a discharge measured with the oscilloscope can be seen in figure 2.6(a). The signal waveform shows periodic oscillations which are due to the inductance of the system. In 2.6(b) the signal is shown after being amplified and shaped by a preamplifier and an amplifier. The signal is composed of a short positive peak followed by a later negative peak.

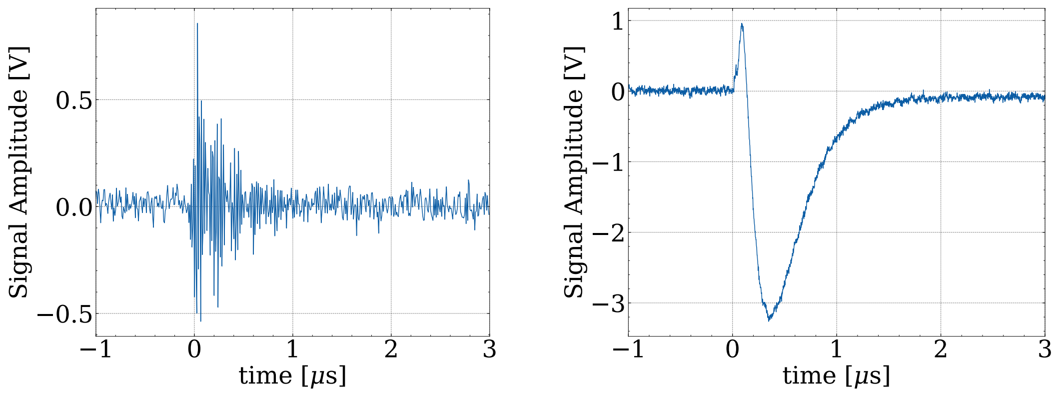

Figure 2.6: Plot of (a) the raw discharge signal and (b) the amplified discharge signal using the oscilloscope

Considering the drift velocity of electrons in Ar-CO_2 (90-10) [23] the signal from the photo coating is expected only a few 100 ns after the initial discharge signal, which leads to the overlapping of both signals. Because of the high amplitude of the discharge signal of a few V, this makes the detection of photon signal difficult. Therefore, the background signal must be suppressed as well as possible.

To reduce the background noise several measures were implemented. To suppress the signal induced by particles created during the discharge a negative blocking field was applied between the THGEM-lamp and wires. Together with the positive drift field, this should ensure that all charged particles are kept away from entering the THGEM. The lamp-THGEM was also changed to a single-hole THGEM to prevent local fluctuations in the signal by restricting the location of the discharge to one hole.
With the implementation of the new readout system, the cables from the anode were running along the setup near the discharge lamp. To prevent the measured signal from being distorted by signal induced directly into the cables, the cables were wrapped with aluminium foil. The signal shapes for the same Pads measured without and with the aluminium shielding are shown in figure 2.7. One can see that the shape of the signal changed. There is only one big positive peak with a tail about 1.5 μs long. It is assumed that the signal comes exclusively from the anode. During measurements, it has been observed that defective cables that lost connection with the anode lead to a signal shape similar to the first unshielded one probably due to the signal being

induced directly into the cables.

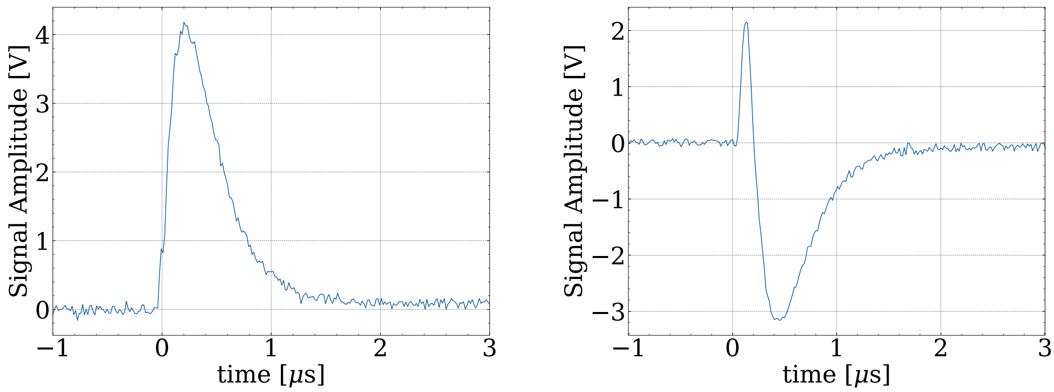

Figure 2.7: Plot of the amplified signal (a) without and (b) with shielding applied to the cables measured with the oscilloscope

With all these measures the signal was still fluctuating a lot, raising more questions. It was unclear if every discharge leads to a "photon event", where an actual signal from the photo coating is created. To investigate that a photo-diode was installed above the THGEM-lamp, but also here the discharge signal dominated with a shape similar to the first discharge signal on the anode. There were two measurements made. In the first one, the diode was embedded in non-conductive material to isolate it from the light, and in the second one it was mounted in the open. Both measurements showed similar signals. It was not possible to isolate individual photon events. Therefore, multiple signals were measured on each pad one by one and compared for coated and uncoated THGEM to see if there was a general difference.

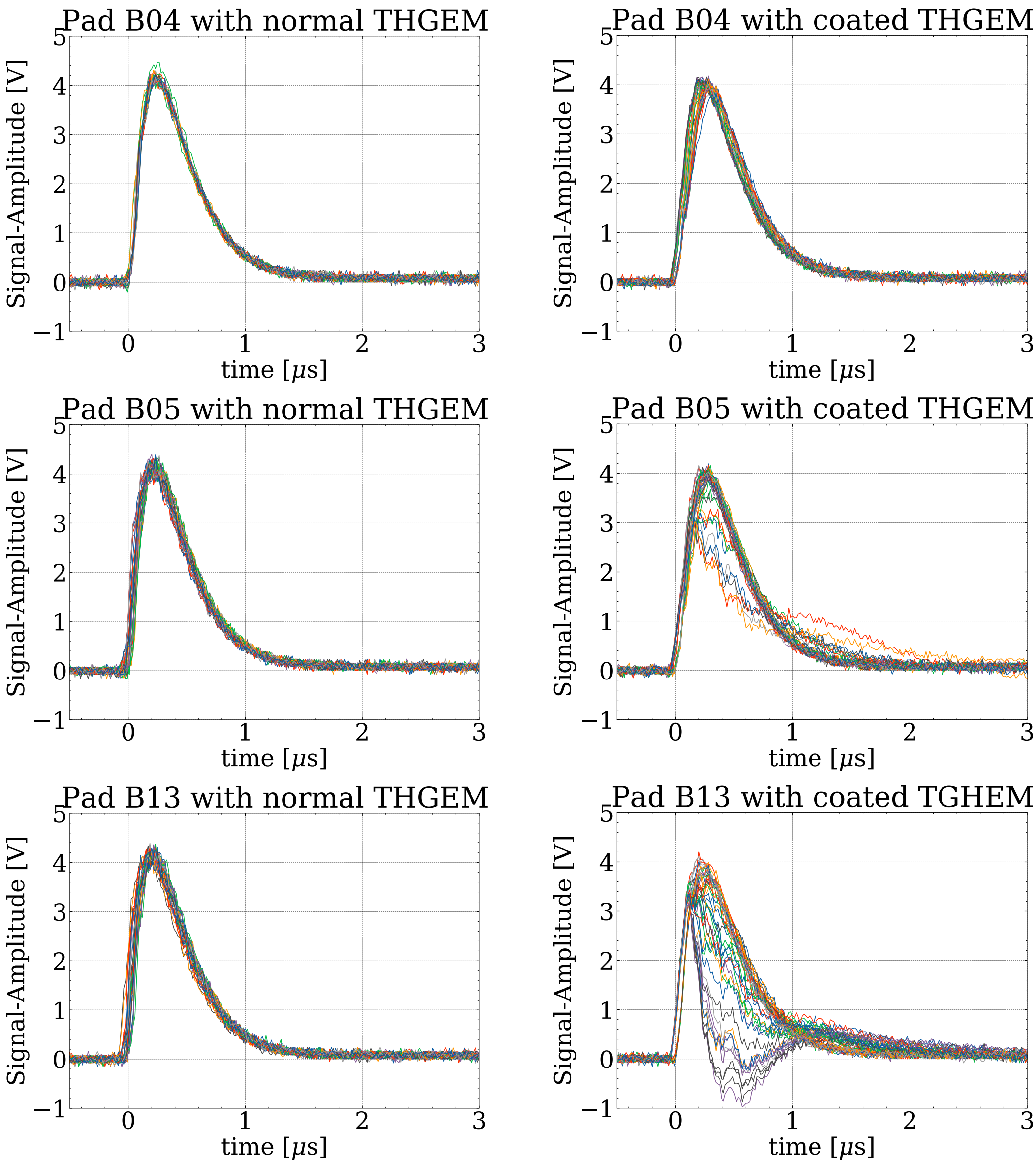

Figure 2.8: Plots of the signal on different pads with (a) uncoated and (b) coated THGEM measured with the osccilloscope

In figure 2.8 one can see the results for some of the pads, with a pad chosen from the coated region in the middle (B05), another from the coated region on the edge (B04), and one from the uncoated region (B13). When comparing coated with normal THGEM, one can see that the signal measured with normal THGEM remains more or less the same across all pads while there are more fluctuations in the measurement with the coated THGEM. These appear primarily on the pads on the edge of the anode. It is unclear if this effect comes from the coating or has another origin. However, for the pads under the coating, there is no significant signal on top of the normal discharge signal. Therefore, this approach was abandoned as it didn't produce the expected results.

As an alternative approach, the currents induced by the signal were measured with the pAmmeter. Measurements with the pAmmeter had some advantages and disadvantages. It was possible to measure up to four pads at the same time, which could be used for simultaneous reference measurement, but also had a smaller time resolution of around 20 Hz. A plot of the signals on different pads together with the reference pad can be seen in figure 3.2. Here, one can see that the signal amplitude differs depending on the pad, but also within a pad, there are different signal shapes and amplitudes. Different signal shapes can be observed. There are basic positive peaks, but also positive peaks followed by negative peaks and completely negative peaks.

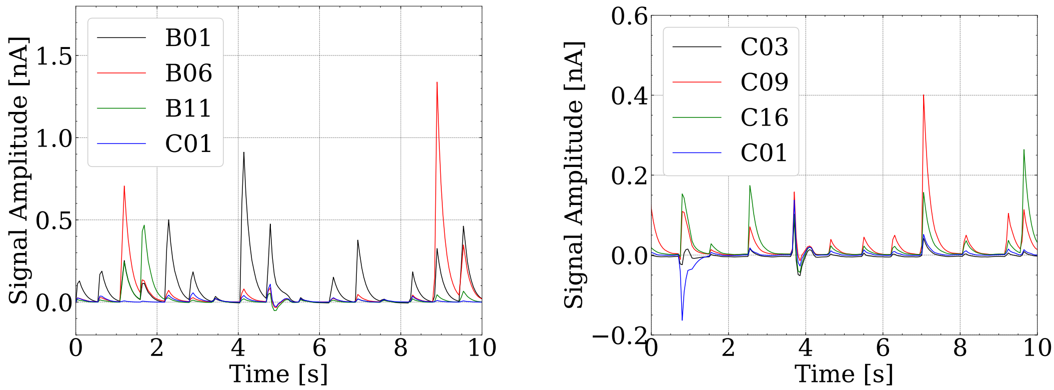

Figure 2.9: Plots of the recorded signals for different pads with the pAmmeter

Here, too, it is not advisable to look at individual signals, since it is not possible to assure that the signal originates from the photocoating. Therefore, the maxima of several signals was considered. As the results seemed more promising, they will be explained in section 4.2. The fields used for the measurements with the discharge lamp can be seen in table 2.2. During the measurements, all fields below the THGEM-lamp were turned on first, and only after enough time to ramp up the THGEMs the discharge lamp was turned on by applying fields to it beyond the Paschen limit.

This was also done for all pads and then compared for coated and uncoated THGEM. The fields used for the measurements with the discharge lamp can be seen in table 2.2. During the measurements, all fields below the THGEM-lamp were turned on first, and only after enough time to ramp up the THGEMs the discharge lamp was turned on by applying fields to it beyond the Paschen limit. The coarse of the current over a time of around 10 min was recorded with the pAmmeter. Then, the amplitude of 500 signals on each pad was extracted.

Field name	electric field / voltage
ΔV_{LAMP} [V]	3100
$E_{cath-wires}$ [V/cm]	800V
E_{Drift} [V/cm]	400
ΔV_{THGEM1} [V]	1000
E_{trans} [V/cm]	2000
ΔV_{THGEM2} [V]	1000
E_{Ind} [V/cm]	4000

Table 2.2: Electric fields/Voltages used in the measurement with the discharge lamp

3 Simulations

Since there are many different parameters, simulations were performed to find optimal conditions. The goal was to minimize IB_{1top} while maximizing the effective Gain. The simulations were carried out using COMSOL [24] and Garfield++ [25]. In this chapter, firstly, the details of the simulations are explained. Later, the reliability of the simulations will be discussed by comparing it to the measurements. In the last part, the results will be discussed.

Comsol is a multiphysics software, where physics-based models can be created and various physical parameters can be simulated. Comsol was used to build a model of the detector and to create a map of the electric fields. These then could be exported to Garfield++ for solving the electron transport inside the applied electric fields. Garfield++ is an object-oriented toolkit aiming to create detailed simulated representations of detectors using gases or semiconductors as a sensitive medium. The main area of application is currently in MPGDs [25]. It can be used to simulate particle transport and avalanche multiplication based on a Monte-Carlo-like system. Furthermore, it can be used to plot field maps as well as electron and ion drift lines. An example of the plots made with Garfield++ for our setup can be seen in 3.1.

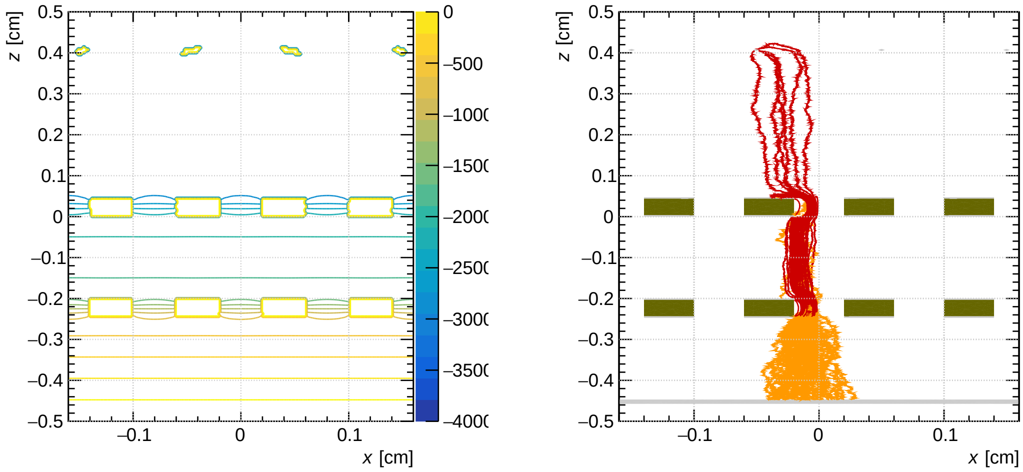

Figure 3.1: Plots of (a) the field map and (b) electron(yellow)/ion(red) drift lines made with Garfield++

3.1 Building the model in Comsol

A simple model of the detector was created with the use of geometrical structures and is shown in figure 3.2. Here it is important that the model is tiling, meaning that one can add copies of the same model together at the outer boundaries, creating a repeating pattern in y- and x-dimension. Like this, the electrodes are expanded creating a homogeneous field, where the avalanches can be simulated later. The distances and proportions were in scale except the cathode-wires-gap distances which were reduced to 5 mm. This was done to reduce the complexity of the system without changing the basic setup below the wires. The different structures were assigned different materials, giving them their respective physical properties. All electrodes were assigned with copper, the THGEM insulator layer with Kapton, and the rest was filled with argon gas. One important physical property has to be added as it's needed later for Garfield++ called the relative permittivity and is defaulted to 1. It can be assigned directly to the different materials. It was set to 1, 4, 1e10 for argon, copper, and Kapton respectively. The next step is to add the electric potentials to the different electrodes. This can be done by adding an electrostatics module to the system and then selecting the different surfaces and applying the respective fields to them. Lastly, periodic conditions have to be added to the x- and y-axis to form a continuum. With the detector complete one can finally implement a study calculating the fields. At this step, a Parametric Sweep was used, where one could select parameter names and assign them to the Parameter value list. One can also choose multiple parameters at a time and the program will go through all possible combinations for the fields. But as the number of combinations and therefore calculation time rises exponentially only up to three parameters were sweep-ed at a time. When the simulation is executed, an electric field map is created for all electrode potential combinations defined. An example of a field map was plotted with field lines in figure 3.3. For use in Garfield++, one has to export the geometry mesh and the field map. The mesh is exported as a Comsol Multiphysics text file (mesh.mphtxt) and contains the structure of the model. The electric field is exported as a text file (field.txt) and contains a list of voltages at different coordinates.

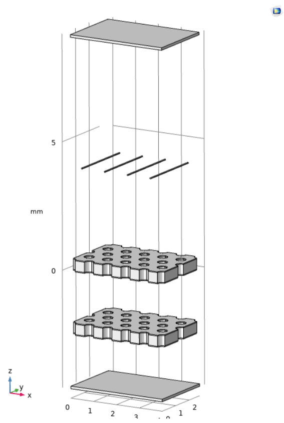

Figure 3.2: The model of the detector built in Comsol

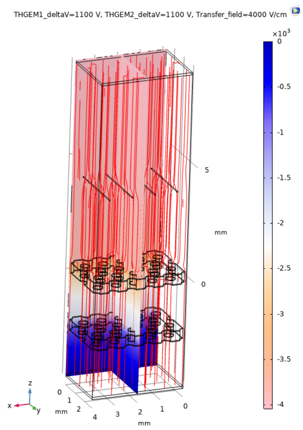

Figure 3.3: Example for a field map plotted together with field lines in Comsol

3.2 Simulating in Garfield++

For simulations in Garfield++, three files need to be imported, describing the structure and fields used in the detector. The first two files are the mesh and field created in Comsol. A third file needs to be imported called "dielectrics.dat" containing the number of materials, a list of the materials with their respective relative permittivity, and a list where the materials are assigned to the different structures built in Comsol. One can choose some properties of the gas like temperature, pressure, composition, and the Penning rate (r_P). The last is a correction coefficient based on the probability of a Penning Transfer to happen. Penning Transfer can occur when an excited noble gas atom transfers its excess energy to an admixture gas, which can lead to an enhanced rate of ionizations. By changing r_P one could adapt the simulations to the measurements done.

In this work, the end position of all created ions and electrons was considered and the number of ions and electrons per primary electron at all electrodes for each primary electron was counted and written down into a text file together with the field used for the simulation, number of total electrons created and number of primary. This was done for 1000 primary electrons per field and for the plots the mean has been taken. A problem that occurred is that the simulation of high gains with many particles took very long to compute, sometimes even leading to crashes and therefore giving a smaller sample. In the same way, when the fields approached 0, the computation time increased to such an extent that it also led to crashes. This could be due to the fact that the particles do not land at electrodes stopping the calculation of movement but wander around for a very long time. There were two things considered to prevent these crashes and to reduce the calculation time. First, the simulation was parallelized, separating a big simulation with 1000 primaries into 10 smaller ones with 100 primaries, which can run simultaneously. Second, the simulation process was partitioned into 2 smaller regions. The first simulation ran only for the area above the center of the transfer gap and therefore only calculated the first avalanche process. Subsequently, all generated electrons with their respective final position, final momentum, and final energy were included as primary electrons in a second simulation covering the entire area. These measures made it possible to reduce the computation time and the frequency of the crashes, but not to prevent them completely. To compare the simulation with the measurements, a common variable had to be found. In the measurement, the current was measured, which wasn't possible in the simulations. However, the current induced onto an electrode is directly proportional to the electric charge of the particle it is induced by. By dividing the measured current by the primary current one gets the ratio of the overall charge of the particles per primary electron. As both ions and electrons carry the charge ± 1 respectively, this can be compared to the simulation, where the same ratio can be achieved by subtracting the number of ions from the number of electrons per primary electron. Therefore we define the ratios R_{meas} for measurement in 3.1 and R_{sim} for simulation in 3.2. These ratios R_{meas} and R_{sim} can be compared to check the accuracy of the simulations.

$$R_{Electrode,Meas} = \frac{I_{electrode}}{I_{primary}} \tag{3.1}$$

$$R_{Electrode,Sim} = \frac{N_{Electrons} - N_{Ions}}{N_{primary}} \tag{3.2}$$

The number of electrons reaching THGEM1top is near zero and very small compared to the number of ions. The same applies to ions at the anode. Therefore R can be used to express the effective gain and IB_{1top} for the simulations:

$$G_{eff,Sim} = R_{Anode,Sim} \qquad IB_{1top,Sim} = \frac{R_{THGEM1top,Sim}}{R_{Anode,Sim}} \tag{3.3}$$

3.3 Penning factor

To find the conditions, where the simulations best reflect the measurements, three field scans were carried out. For each field scan the measurements were accompanied by multiple simulations with varying r_P. The first and third ones utilized the normal double THGEM setup, where $\Delta V_{THGEM1/2}$ were swept respectively. In the second field scan a single THGEM setup was imitated by setting all fields below the first THGEM to 0 V/cm, while sweeping ΔV_{THGEM1}. In table 3.1 one can see the fields and voltages used for the three field scans. In all three measurements, the currents on the four THGEM-electrodes were measured for around 5 min while varying the swept THGEM-ΔV from 0 V to 1100 V in 100 V steps. As the THGEMs need some time to charge up around 30 min was waited between measurements. In all plots in this section, the measurements were marked by diamonds while the simulations were marked by lines. The different colors refer to different electrodes/r_P.

Field name	Field Scan 1	Field Scan 2	Field Scan 3
$E_{Cath-Wires}$ [V]	200	200	200
E_{Drift} [V/cm]	400	400	400
ΔV_{THGEM1} [V]	swept	swept	800
E_{Trans}[V/cm]	2000	0 V/cm	2000
$\Delta V_{THGEM1/2}$[V]	800	0	swept
E_{Ind} [V/cm]	0	0	4000

Table 3.1: The electric fields/Voltages used for the three Simulation-Measurements

For the first measurement, a coarse scan in simulations was made. The measured R-values together with the simulated ones can be seen in 3.4. One can see that by lowering r_P the ratios on all electrodes decrease as well, which makes sense as by lowering r_P the probability of additional ionizations decreases. However, the different electrodes are impacted differently. For $r_P = 0.51$ the ratios for THGEM1top and THGEM2top are nearly the same, but by decreasing r_P, fewer ions seem to get to THGEM2top, which is also the case in the measurements. From this coarse scan, r_P could be contained at between 0.21 and 0.31, as these simulations reflect the measurements the best.

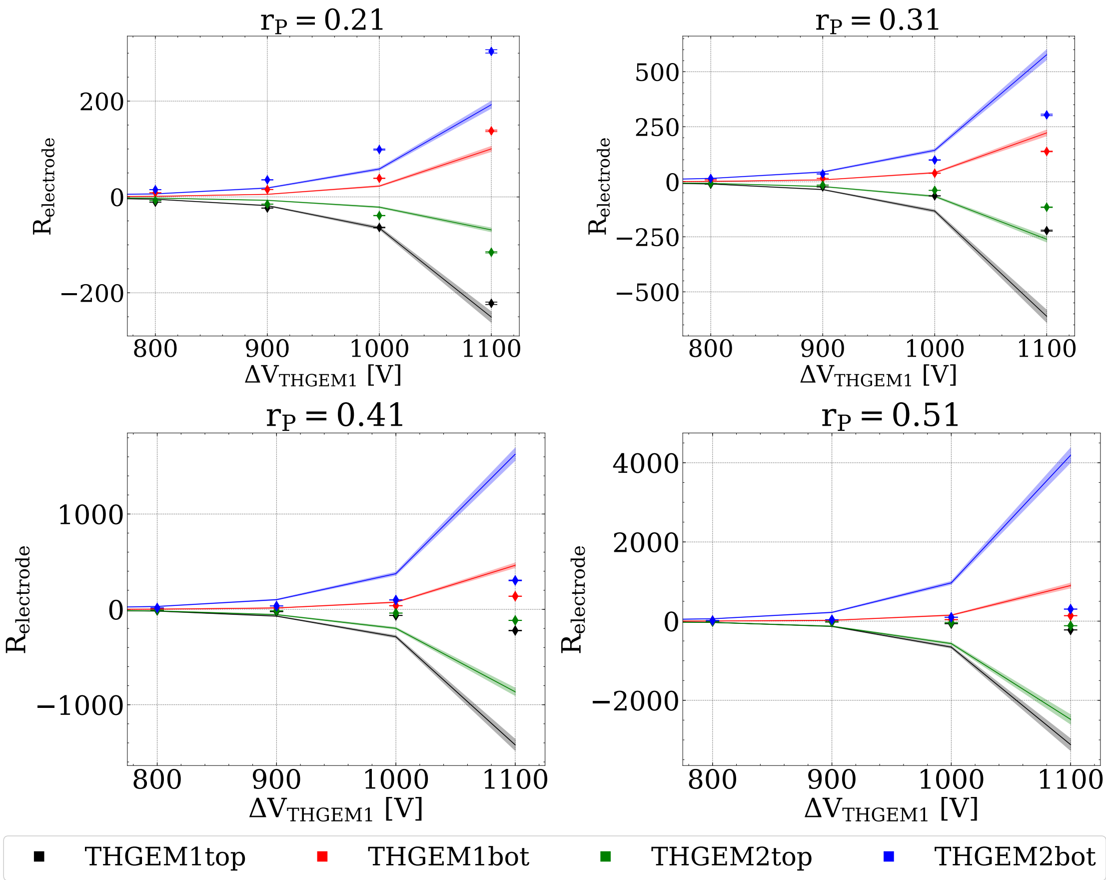

Figure 3.4: Plot of the R-values of all electrodes for measurement and simulations with $r_P = 0.21, 0.31, 0.41, 0.51$

For a more accurate result, simulations with $r_P = 0.22, 0.23, 0.24, 0.25$ were made for all three measurements. In figures 3.5-3.7 a plot of the absolute R-values for all four THGEM electrodes can be seen. Here, the different colors mark the different simulations. One can see that the result isn't clear. The accuracy of the simulation to represent the Measurements varies for each electrode and measurement. For further simulations, $r_P = 0.22$ was chosen as it reflects the measurements most stable across all measurements.

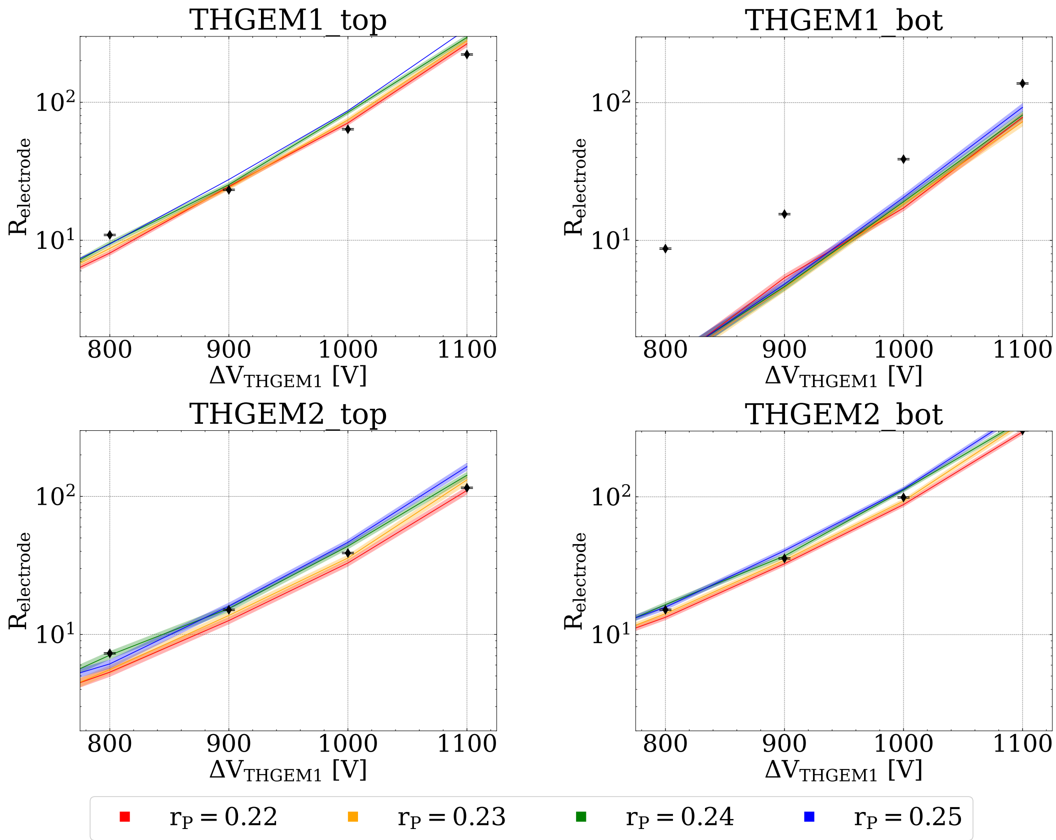

Figure 3.5: field scan 1: plot of the absolute R-values on all THGEM electrodes for measurement and different simulations

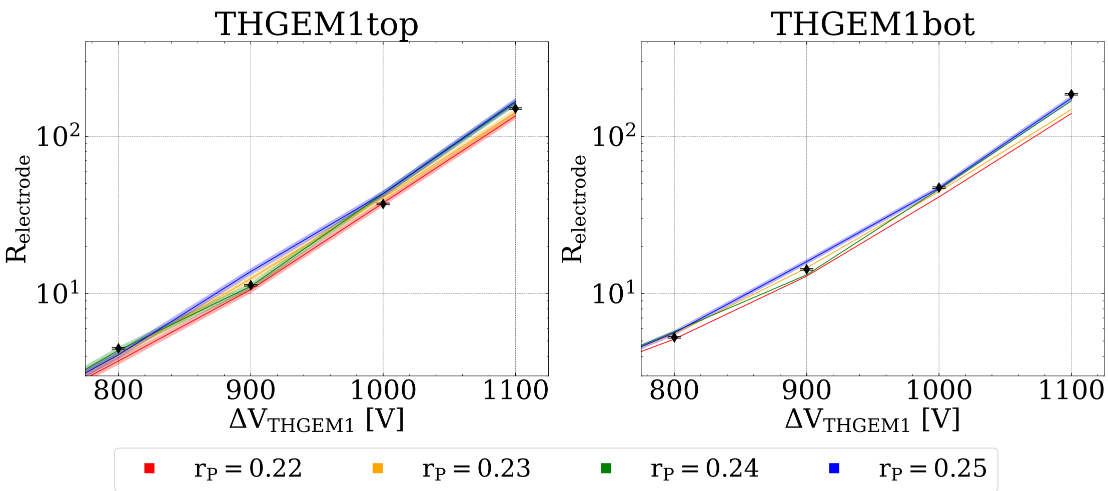

Figure 3.6: field scan 2: plot of the absolute R-values on the two THGEM1 electrodes for measurement and different simulations

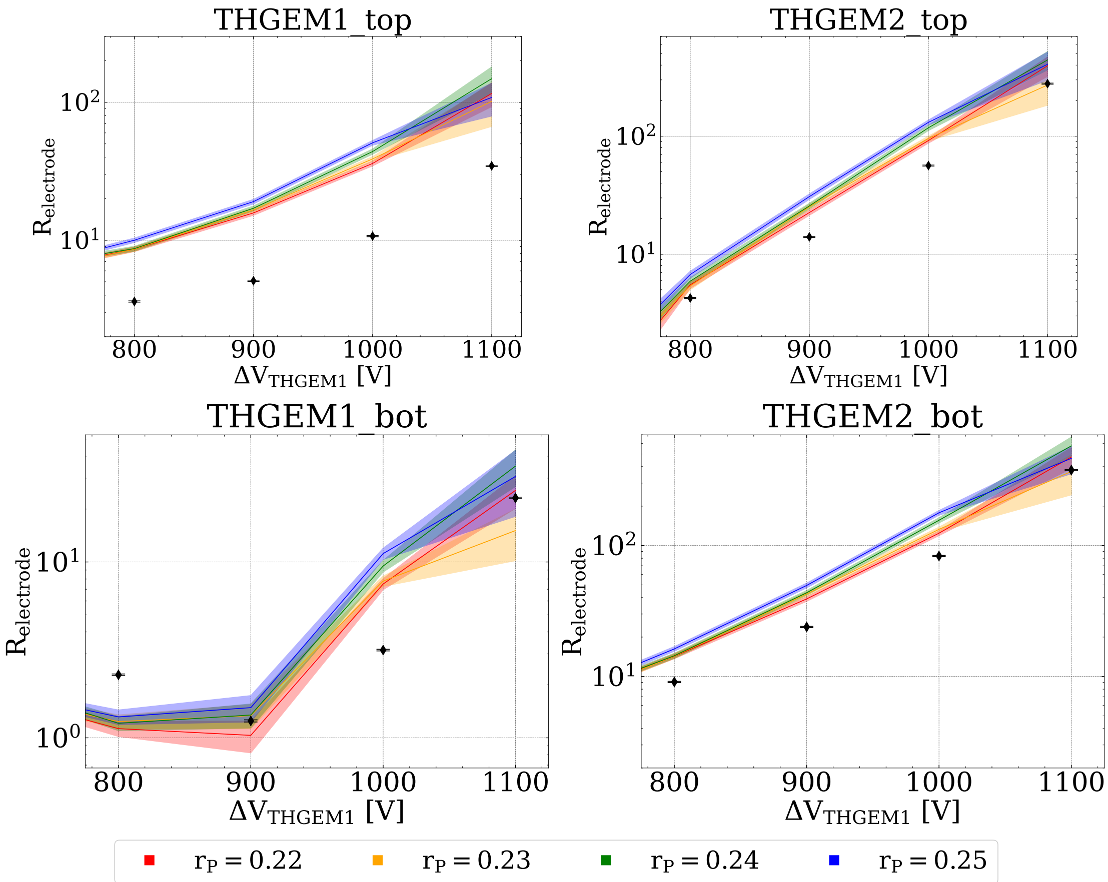

Figure 3.7: field scan 3: plot of the absolute R-values on all THGEM electrodes for measurement and different simulations

A last control measurement was done measuring additionally the currents of wires and the anode. On top of changing the voltage of the THGEMs, the transfer field was also changed. The according simulations were done with $r_P = 0.22$. In figure 3.8 one can see the plotted R-values. Again, the simulation approaches the measurement differently for the different electrodes. Further changing r_P wouldn't lead to better results as small changes would only change the absolute values equally, which would improve the results for some electrodes but worsen the results for others. Especially $R_{THGEM1top}$ isn't reproduced that well by the simulations, which is unfavorable as the ion bombardment of THGEM1top is one of the quantities we want to optimize. However, the simulations show the right tendencies and therefore can be a good way towards the optimal fields.

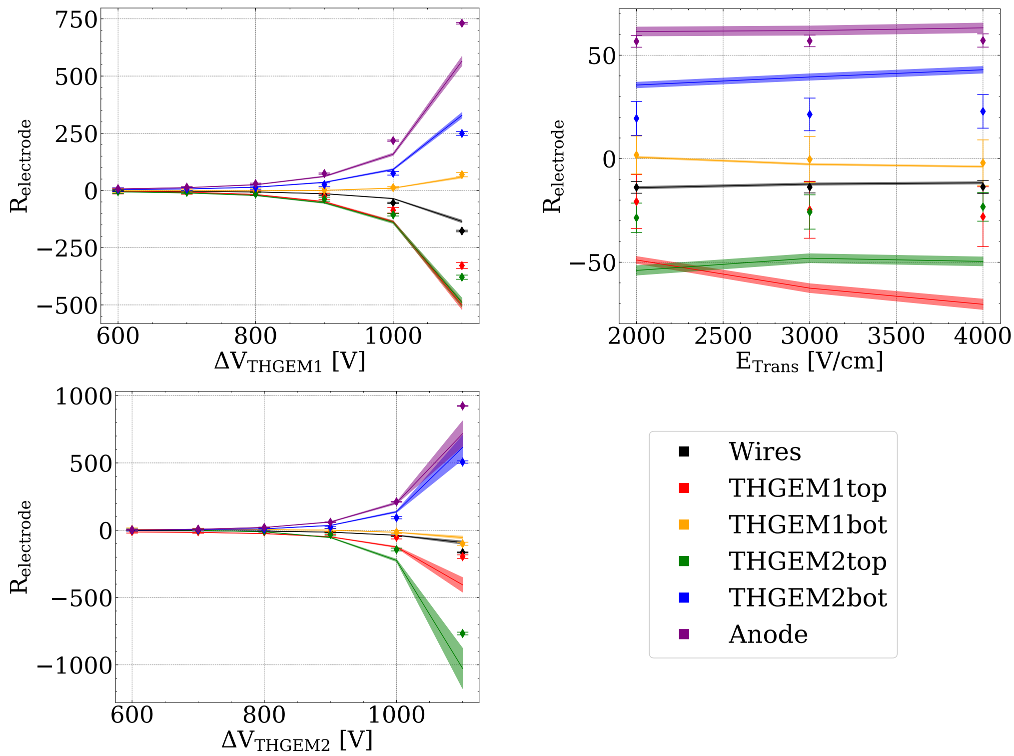

Figure 3.8: Plot of the R-values of all electrodes for measurement and simulation with $r_P = 0.22$

3.4 Field scans

This section discusses the different field scans made to find optimal conditions. Here we examine the absolutes of R_{Anode} and $R_{THGEM1top}$, which represent the number of electrons/ions at the anode/THGEM1top. With these both G_{eff} and IB_{1top} can be calculated using the equations 3.3. During the simulations, one field was changed while the others remained the same. The used fields for the simulation can be seen in table 3.2.

field name \ scanned field	E_{Drift}	ΔV_{THGEM1}	ΔV_{THGEM2}	E_{Trans}	E_{Ind}
$E_{Cath-Wires}$ [V/cm]	0	200	200	0	0V
E_{Drift} [V/cm]	scan	400	400	400	400
ΔV_{THGEM1} [V]	800	scan	1000	800	800
E_{Trans} [V/cm]	2000	2000	2000	scan	2000
ΔV_{THGEM2} [V]	1000	1000	scan	1000	1000
E_{Ind} [V/cm]	4000	4000	4000	4000	scan

Table 3.2: The electric fields/Voltages used for the simulated field scans

The simulations for the drift/transfer/induction fields were done at lower gain to speed up the simulation and to avoid crashes, reducing the sample size. Smaller simulations with higher gain showed similar results.

3.4.1 Drift field

The drift field is responsible for leading primary electrons to the holes of the first THGEM. In this case, it can also be used for keeping ions away from the sensitive photo coating. In figure 3.9 (a) the absolute of R_{sim} of anode and THGEM1top can be seen. It indicates that the effective gain represented as R_{Anode} has a maximum around 0 V/cm and drops when a field is applied. This effect comes from the fact that electrons are not created all over the drift gap but by the photo coating on top of THGEM1. A negative field can lead the electrons away from the THGEM whereas a positive field can trap the electrons between the holes of the THGEM. In both cases, fewer electrons are introduced into the THGEM holes, which is reflected in a drop of gain. With fewer primary electrons induced to the system, the ions at THGEM1top decrease. Therefore for maximum gain E_{Drift} would be set to 0 V/cm. But if observing $R_{THGEM1top}$ it can be determined that it also has a maximum at 0 V/cm and drops when fields are applied. This is a direct consequence of the fall in total gain since fewer electrons being introduced to the avalanche process means fewer ions being created. However, the drift field still has an impact on the ions, which is reflected in the coarse of IB_{1top} shown in figure 3.9 (b). For negative fields, nearly all ions leaving THGEM1top are caught on it leading to an IB_{1top} of about 100 %. With increasing positive drift fields more and more ions are led away, therefore reducing IB_{1top}.

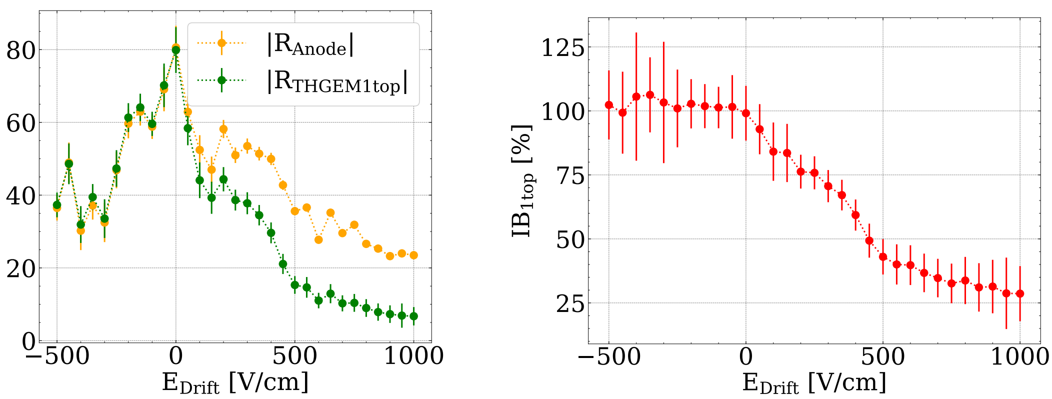

Figure 3.9: Plot of (a) the absolutes of R_{Anode} (yellow) and $R_{THGEM1top}$ (green) and (b) IB_{1top} for changing drift field

Both maximizing the effective gain and minimizing IB_{1top} at the same time is not possible. Here, one should also consider the IBF, mentioned in section 2.2.2. In a higher drift field, more ions are released into the drift gap, which would be beneficial to spare the coating but would also impact the overall detector performance negatively. The drift field was set to 400 V/cm, where the effective gain is about 65 % of the maximum possible gain and the IB_{1top} lies at around 60 %.

3.4.2 THGEMΔV

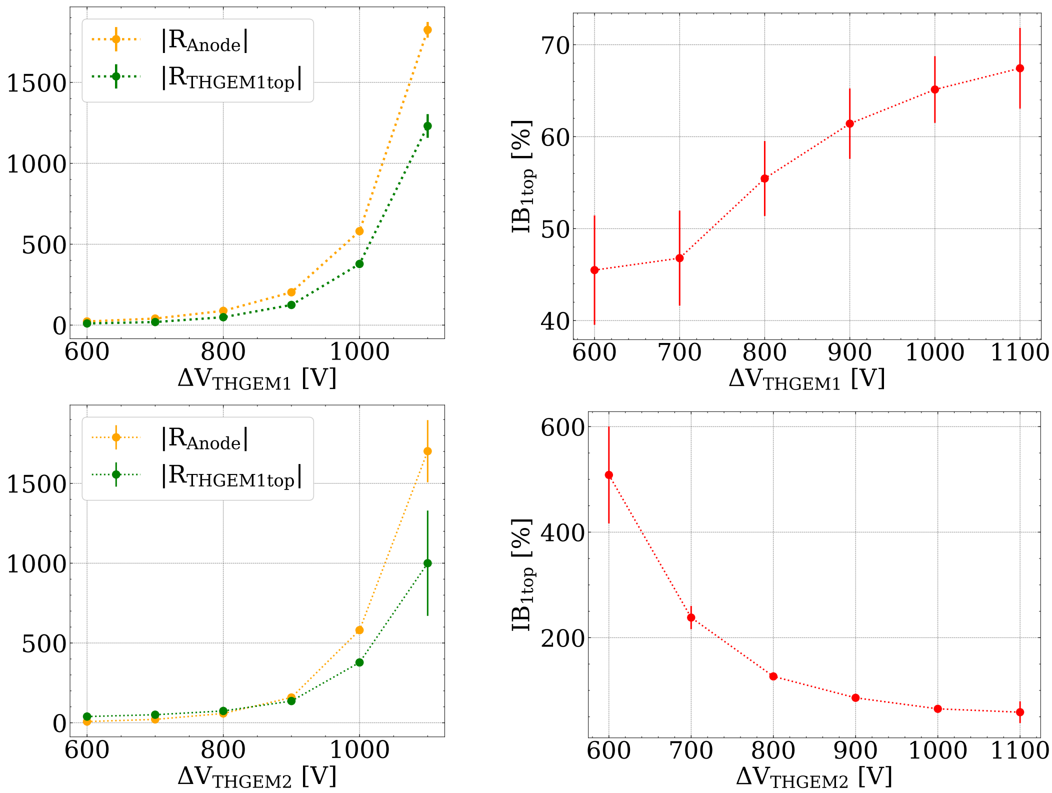

Figure 3.10: Plot of (left) the absolutes of R_{Anode} (yellow) and $R_{THGEM1top}$ (green) and (right) IB_{1top} for changing ΔV_{THGEM1} (top) and ΔV_{THGEM1} (bottom)

The voltage difference applied to both electrodes of a THGEM is largely responsible for the avalanche multiplication process. The number of electrons at the anode rises exponentially with increasing field in both THGEMs. The same applies to ions at THGEM1top. However, there are differences between the two THGEMs when looking at the IB_{1top}. For THGEM1 it rises with increasing field, whereas it decreases for THGEM2. To investigate on that in figure 3.11 a scatter plot of $R_{THGEM1top}$ against R_{Anode} for both changing ΔV_{THGEM1} and ΔV_{THGEM2} has been made. The values for ΔV_{THGEM1} are indicated by the colors while the values for ΔV_{THGEM2} are indicated by the different shapes. One can see a difference in the gradient. By changing ΔV_{THGEM1} while keeping ΔV_{THGEM2} constant $R_{THGEM1top}$ increases more with the rise of R_{Anode} than doing it the other way around. Also R_{Anode} seems to increase more by raising the fields in the second THGEM. This can be explained by the loss of THGEM1-avalanche electrons in the transfer gap, resulting in fewer electrons entering the avalanche process of the second THGEM. The same applies to the ions created in the second THGEM. They are more likely to get caught on top of the second THGEM and therefore not reach the first THGEM.

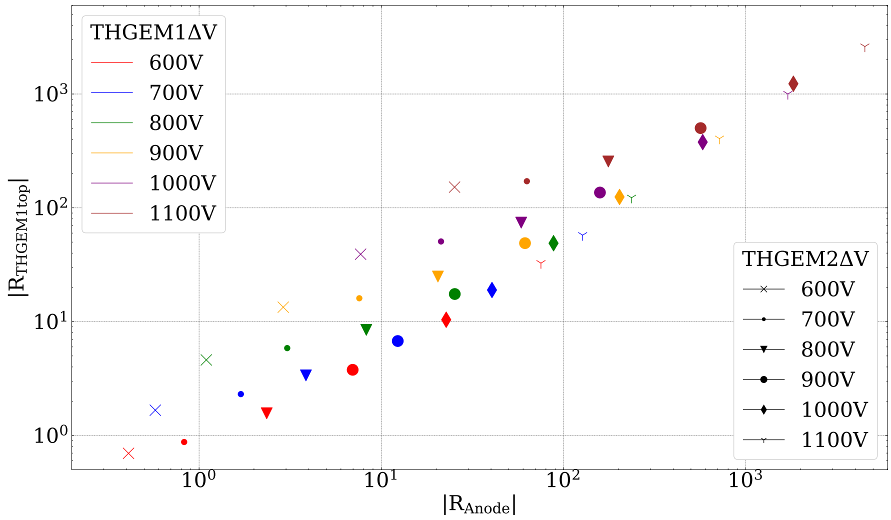

Figure 3.11: $R_{THGEM1top}$ plotted against R_{Anode} for different values of ΔV_{THGEM1} (shapes) and ΔV_{THGEM2} (colors)

The second THGEM contributes more significantly to the effective gain than the first one. So one should consider first increasing ΔV_{THGEM2} as high as possible without discharging while keeping ΔV_{THGEM1} a bit lower and increasing ΔV_{THGEM1} only when even more gain is needed. The measurements have shown that the discharges for a single THGEM begin to appear between 1000 V and 1100 V.

3.4.3 Transfer field

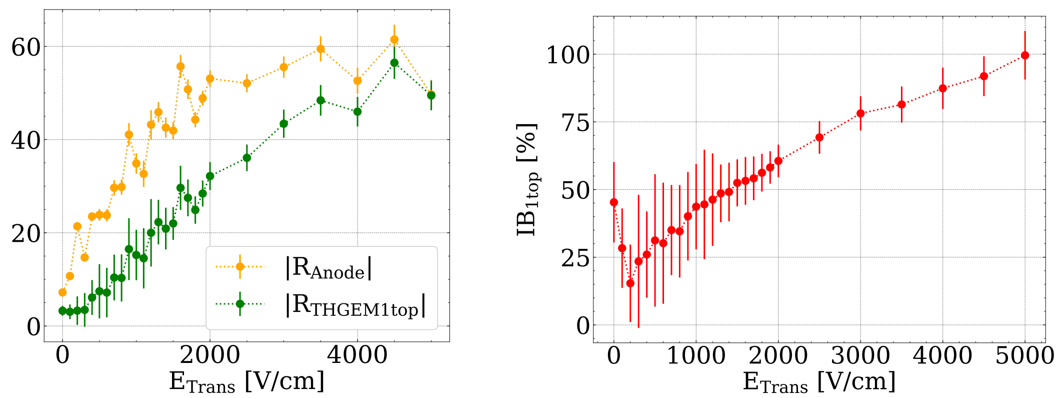

Figure 3.12: Plot of (a) the absolute R-values of anode (yellow) and THGEM1top (green) and (b) IB1t with changing transfer field

The transfer field is responsible for leading the avalanche electrons of the first THGEM to the second one. It also affects the ions created in the avalanches of THGEM2. As shown in figure 3.12 (a) both R_{Anode} and $R_{THGEM1top}$ rise with increasing transfer field. This is as expected since both electrons and ions are more strongly directed and less likely to get lost in the transfer gap. However, R_{Anode} saturates at around 2000 V/cm while $R_{THGEM1top}$ keeps rising until around 3500 V/cm. The field required for most electrons to reach the second THGEM is smaller than the one for ions, which leads to a faster saturation. This can be observed at the coarse of IB_{1b} in 3.12 (b). It first decreases as low fields are only strong enough for the electrons and then rises as the field gets strong enough to influence the ions as well. Here, it has to be pointed out that the simulations crashed a lot for lower fields, which is reflected in the rather large errors as a lot of particles wander around dragging out the simulation. The gain remains mostly constant for fields between 1800 V/cm and 5000 V/cm, while the IB_{1t} keeps rising in this range. Therefore, the transfer field of 2000 V/cm was chosen for optimal conditions.

3.4.4 Induction field

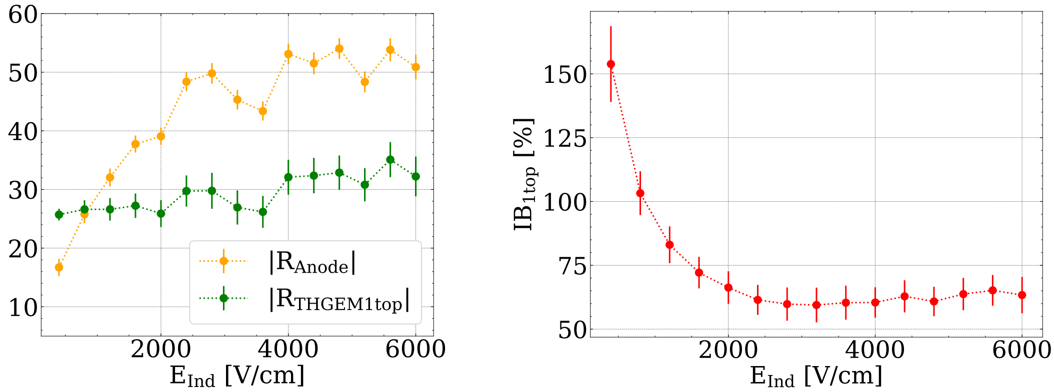

Figure 3.13: Plot of (a) the absolute R-values of anode (yellow) and THGEM1top (green) and (b) IB1t with changing induction field

The induction field doesn't directly affect the avalanche process but ensures that the avalanche electrons reach the anode. Therefore, $R_{THGEM1top}$ remains more or less constant when changing the induction field. R_{Anode} on the other hand rises with increasing E_{Ind} until it saturates at around 2400 V/cm. This can also be seen in figure 3.13 (b) where it lowers until 2400 V/cm and then remains constant. For optimal conditions, the induction field can be somewhere between 2000 V/cm and 6000 V/cm, whereby lower fields usually are better to spare the electrodes.

3.5 Optimal field configuration

In table 3.3 the optimal fields predicted by the simulations can be seen. It is important to note, as was pointed out in section 3.3, that the simulations may not perfectly emulate all aspects of the actual measurements. Therefore these results should be considered as a guideline rather than an exact representation of the measurements.

Field name	electric field / voltage
$E_{Cath-wires}$ [V/cm]	-
E_{Drift} [V/cm]	400
ΔV_{THGEM1} [V]	1000-1100
E_{Trans} [V/cm]	2000
ΔV_{THGEM1} [V]	800-1100
E_{Ind} [V/cm]	2000-4000

Table 3.3: Optimal field configuration acquired in the simulations

Dependent on how much gain is needed $\Delta V_{THGEM1/2}$ can be adjusted. Thereby one should first increase ΔV_{THGEM2} to the maximum without discharging before increasing ΔV_{THGEM2}. For the deuterium lamp measurements, a lower gain was sufficient, since in measurements with the coated THGEM high currents appeared and a higher gain would have led to the currents exceeding the range of the pAmmeter. Simulations with the fields used in that measurement expected an effective Gain of around 40 and an IB_{1top} of around 65 %. The discharge lamp measurements didn't exceed the range of the pAmmeter, therefore maximum $\Delta V_{THGEM1/2}$ were used. Due to the addition of the negative $E_{Cath-Wires}$ above the wires E_{Ind} was increased to keep all voltages in the range of the used HV-power supply. Simulations with fields used in the discharge lamp measurements estimated an effective gain of around 350 and an IB_{1top} of around 80 %.

4 Results

4.1 Deuterium lamp

In the measurements with the deuterium lamp, the effect of the photocoating on the individual pads of the anode was considered. Measurements with the uncoated THGEM were compared with the coated THGEM and, for measurements with the coated THGEM, pads under the coated areas were compared with pads under the uncoated areas.

A heat map of the normalized currents measured with an uncoated THGEM can be seen in figure 4.1. The shape is as expected as the light source can be seen as a point-like radiator emitting light in all directions. The intensity on a point in space is indirectly proportional to the square of the distance from the source.

Figure 4.1: Heat map of the measured currents with multi-pad anode, deuterium lamp, and uncoated THGEM, currents in [nA]

In figure 4.2 amplitude was plotted against the distance of the center of the pad from the projection of the position of the lamp into the readout plane. This was done for all pads together with the mean for pads with same distance. One can see that there are large variations between the pads and not all pads fall within the range defined by the error bars. This could indicate that the gain isn't uniform across the whole area.

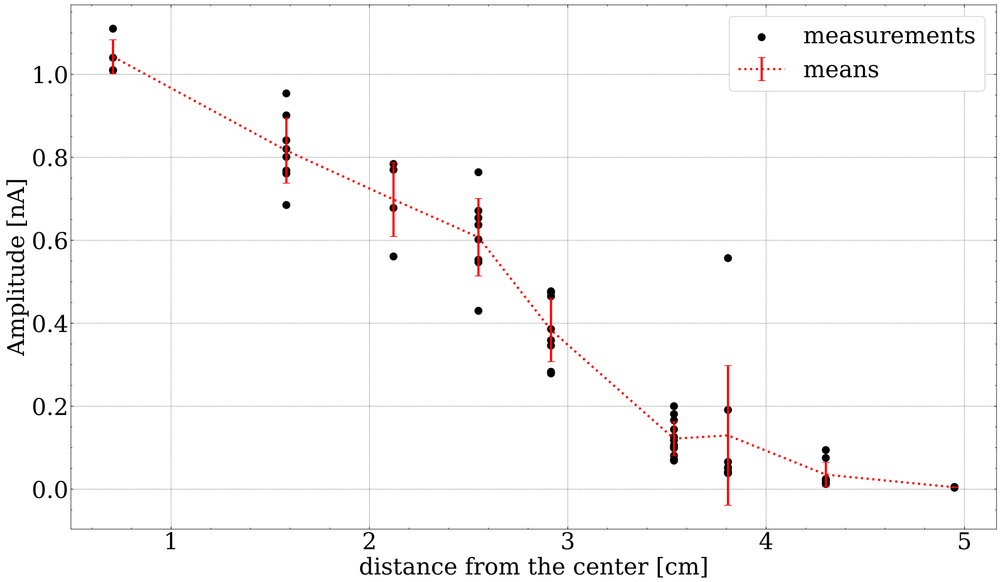

Figure 4.2: Plot of the measured currents together with the mean depending on the distance between the center of the pads from the projection of the lamp onto the readout plane.

Some outlier pads are observed, such as pad D9, where the current measured was higher than expected. This was observed not to be a reoccurring effect as it changed from measurement to measurement. It is suspected to be related to the cabling of the readout system and is under investigation.

The four pads directly under the light source measured currents of around 1 nA, while most outer pads only measured a few pA.

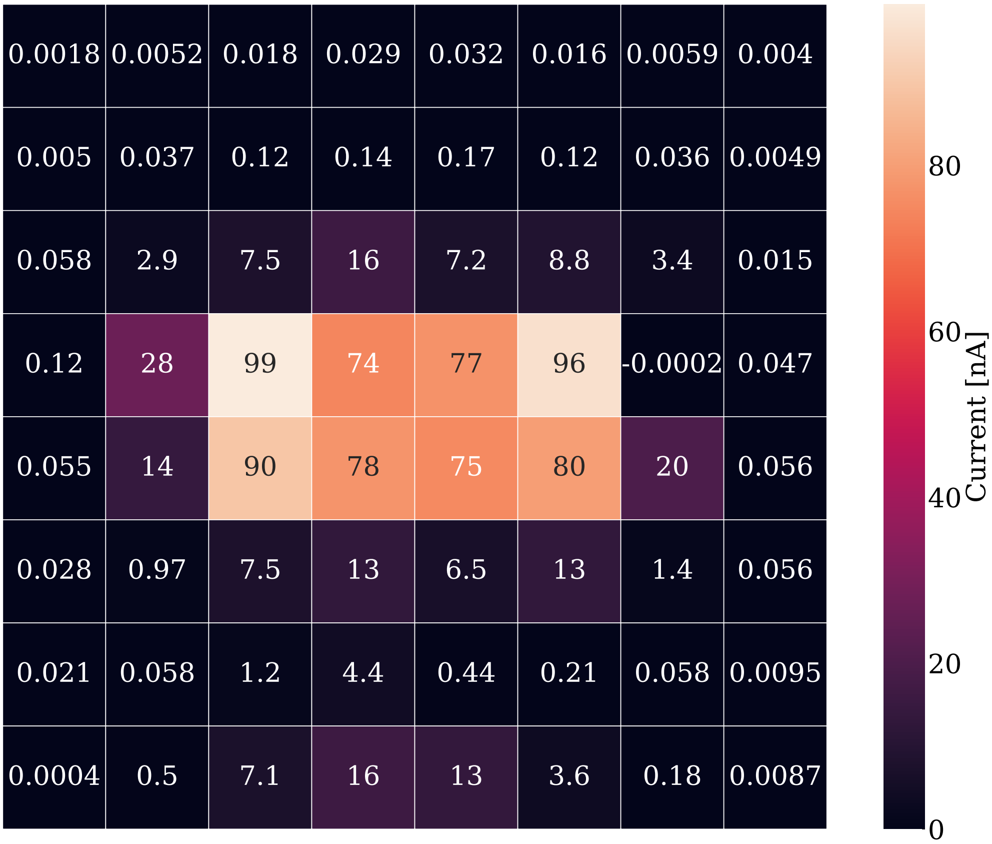

Figure 4.3: Heat map of the measured currents with multi-pad anode, deuterium lamp, and coated THGEM, currents in [nA]

Figure 4.3 shows the normalized current-heat map of the measurement with the coated THGEM. The pads directly under the middle coated region clearly stand out with currents of 70-100 nA, where the outer pads measure the highest currents. This is surprising as the light intensity directly under the lamp is the highest and therefore one would expect the highest currents there. One possible explanation for this is that the coating is very old (coated over a year ago) and impurities may have formed over time, resulting in different quantum efficiencies across the coated area. The pads surrounding the middle eight also measure higher currents of around $7 - 30nA$ as they are partially under the coating. Here applies the higher the overlap with the coated area the higher the current. For Pad D14 no currents were measured due to a connection loss inside the cables. This connection loss also leads to the pad not being grounded, as the grounding is also applied through the cables, which could have an impact on the surrounding pads. For the pads under the lower coated region currents of around $3 - 17nA$ were measured. Here, the highest currents appear in the middle two pads. The surrounding pads, partially under the coated area, also have a higher current. But here, compared to the middle coating, the currents don't fully rise with the portion of overlap with the coated area as geometrical factors also play a role.

Figure 4.4: Heat map of the normalized ratios of currents measured with coated and uncoated THGEM

To get a better look at the efficiency of the coating without geometrical factors the measured currents with coating were divided by the respective currents without coating. As the intensity of the lamp may have been different for the two measurements a factor was multiplied. For this, the ratio of the mean currents on the four outermost pads was chosen as these pads would be affected the least by the coating. A heat map of the normalized currents can be seen in figure 4.4. The coated regions are clearly distinguishable. For all pads that are fully under the coated regions, the coating increases the currents by a factor of 75.5 ± 19.2. However, there are major variations between the pads. The outer pads of the middle coating, which already measured higher currents with the coated THGEM, have even higher ratios due to smaller currents during the measurement with the uncoated THGEM. There can also be seen a trend on the lower coating where the Ratio increases from right to left.

4.2 Discharge lamp

As pointed out in section 2.3 it was not possible to identify single photon pulses using a THGEM-lamp as source. However, the general effect of the photo-coating on the discharge signal measured with the pAmmeter can be discussed.

Across all pads, higher currents were measured with the uncoated THGEM. This could be due to a difference in gain between the two different THGEMs. To still be able to compare these two measurements the signal amplitude was normalized by dividing it with the mean amplitude of the reference pad for each measurement. The normalized height distribution for sector B with coated (orange) and uncoated (blue) THGEM can be seen in figure 4.5.

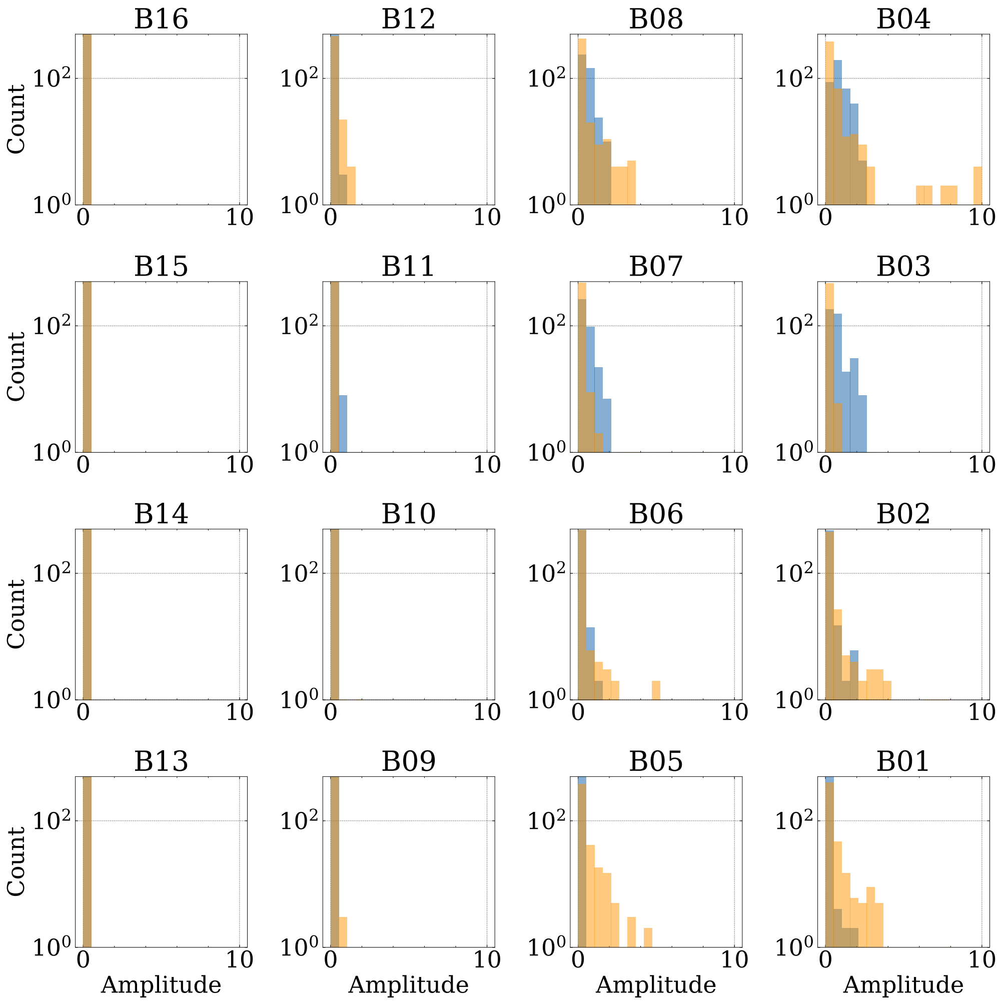

Figure 4.5: height distribution of 500 peaks per pad in sector B measured with the pAmmeter

There are noticeable differences between the measurements with coated and uncoated THGEM. For the uncoated THGEM, higher currents were measured on pads closer to the hole of the THGEM-lamp. The amplitude distribution thereby appears broad, meaning that the different amplitudes are more uniformly distributed. For the coated THGEM on the other hand the strongest peaks were measured at the pads under the coated regions. They are less evenly distributed, meaning that most peaks are at lower currents and only a few higher currents occur. This could be indicating the photon events we are looking for, but without suppressing the background signal it is difficult to prove.

The measurement with the normal THGEM indicates a dependence of the amplitude on the distance from the source of the discharge. For further investigation, a heatmap displaying the normalized means of the peak height for sector B is shown in figure 4.6 (a). There, it can be observed that on average, higher currents are measured on the pads in the middle of the anode and the further the pads are away the lower the currents get. However, during measurements with the oscilloscope, no such dependence was observed. Therefore, the same measurement was done with the raw discharge signal. This was achieved by only applying the drift field whereby no amplification can happen. For this measurement also a heatmap was made and is shown in figure 4.6 (b). Here, the amplitudes are in general very small and are more evenly distributed across the pads. This indicates that the raw discharge signal does not depend on the position and that the differences in the signal probably come from electrons created during the discharge. For the raw signal measurements, it was observed that the measured currents were influenced mostly by the time at which the currents were measured. The three pads which are measured at the same time always have similar currents amongst each other. This was not the case with the other measurements with higher currents. Therefore, the measurement method is not so well suited for measurements of small signals.

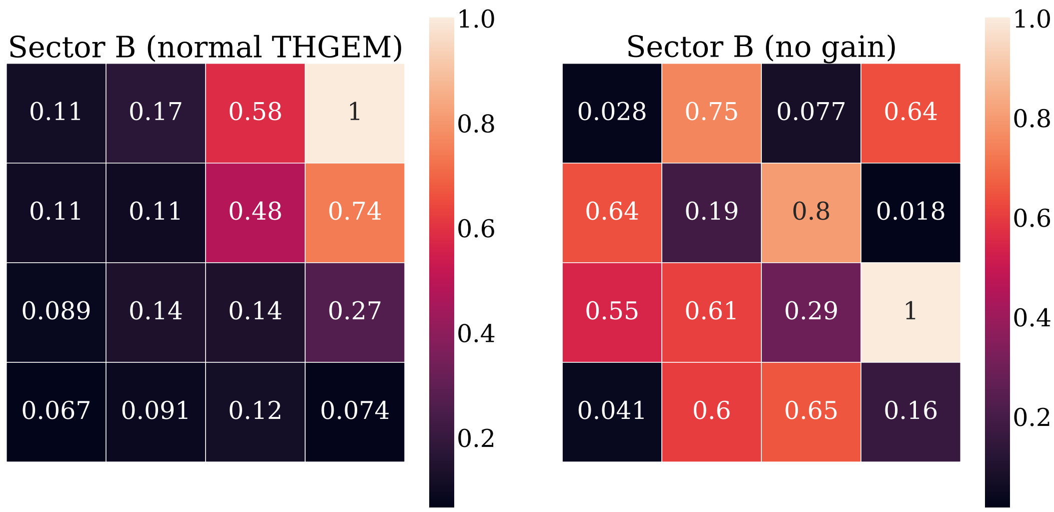

Figure 4.6: normalized heatmap of the means of the measured currents with the normal THGEM (a) with and (b) without gain

5 Conclusion and outlook

In the course of this thesis, a multi-pad THGEM detector setup has been tested for the detection of light in the VUV spectrum. It uses two THGEMs, the upper of which has been partially coated with a CsI reflective photocathode, and was read out with a newly developed multi-pad anode. First, simulations of different electric field configurations and resulting electron transport properties in the detector were carried out to find the optimal operating conditions. Thereby it was tried to maximize the effective gain while keeping the ion bombardment of the photo-cathode as low as possible. These simulations were accompanied by measurements to evaluate their validity. It has been shown that these simulations do not fully reproduce the measurement, but nevertheless point in the right direction. From the studies, field configurations with effective gains of up to 350 were demonstrated to be reachable during stable operation, while also keeping the IB_{1top} below 80 %. Next, a new multi-pad anode was designed and implemented into the setup along with a new readout system making it possible to read out 64 different pads with easy accessibility. The new readout anode mitigates the issue observed in previous studies using a single pad large area anode for readout, where it becomes exceedingly difficult to disentangle real signal and background contributions, especially prevalent in the outer edges of the detector.
The new setup was tested for photon detection with different light sources. Measurements with a deuterium lamp showed that for a continuous light beam, it is possible to measure the effect of the photo-coating on individual pads by comparing measurements with an uncoated and coated THGEM. Lastly, measuring photon pulses instead of a continuous light input was tested. Since there are no LEDs capable of producing light in the VUV spectrum, another source had to be found. For this purpose, a discharging THGEM (THGEM-lamp) was utilized, where the light output from discharges is known to extend into the VUV spectrum. With an oscilloscope and a pAmmeter the signal was measured at different pads on the readout plane and was compared for uncoated and coated THGEM. However, it turned out, that the THGEM-lamp is a poor source, as the discharge signal suppresses the expected photon signal. With the oscilloscope, no difference could be observed between the signal measured for uncoated and coated THGEM. The measurements with the pAmmeter were more promising since effects were observed which indicated a measurement of a photon pulse. Nevertheless, it was not possible to prove whether it was actually a photon pulse. Therefore, in order to use a THGEM-lamp as a pulsed photon source further investigations would be needed., where a main challenge would be to suppress the electrical signal from the discharge.
In summary, the work conducted in the scope of this thesis demonstrates the benefits of using a readout system with spatial granularity in systematic studies aiming to characterize different photocathode materials or detector configurations aiming to be used in future MPGD based photon detectors.

Acknowledgments

First of all, I want to thank Prof. Laura Fabbietti for the great opportunity to learn and work in her friendly group. A special thanks goes to my supervisor Berkin Ulukutlu who guided and supported me all the way throughout this thesis. I also want to express my gratitude to Dr. Piotr Gasik for all his grateful advice. Furthermore, I want to thank the other members of the GEM-crew including Thomas Klemenz, Henrik Fribert, and Anil Adıgüzel, who were always happy to help. Finally, I want to thank my friends and my family who always supported me.

List of Figures

List of Tables

Bibliography

[1] J. S. Townsend. "The Conductivity produced in Gases by the Motion of Negatively-charged Ions". In: *Nature* 62 (Aug. 1900), p. 340. ISSN: 1476-4687. URL: https://doi.org/10.1038/062340b0.

[2] P. D. Group, P. A. Zyla, R. M. Barnett, and e. a. Beringer. "Review of Particle Physics". In: *Progress of Theoretical and Experimental Physics* 2020.8 (Aug. 2020), p. 083C01. ISSN: 2050-3911. DOI: 10.1093/ptep/ptaa104. eprint: https://academic.oup.com/ptep/article-pdf/2020/8/083C01/34673722/ptaa104.pdf. URL: https://doi.org/10.1093/ptep/ptaa104.

[3] F. Paschen. "Ueber die zum Funkenübergang in Luft, Wasserstoff und Kohlensäure bei verschiedenen Drucken erforderliche Potentialdifferenz". In: *Annalen der Physik* 273.5 (1889), pp. 69–96. DOI: https://doi.org/10.1002/andp.18892730505. eprint: https://onlinelibrary.wiley.com/doi/pdf/10.1002/andp.18892730505. URL: https://onlinelibrary.wiley.com/doi/abs/10.1002/andp.18892730505.

[4] F. Sauli. "GEM: A new concept for electron amplification in gas detectors". In: *NIM A* 386 (1997), p. 531. URL: https://doi.org/10.1016/S0168-9002(96)01172-2.

[5] CERN. *ALICE experiment at CERN*. 2023. URL: https://home.cern/science/experiments/alice.

[6] CERN. *COMPASS experiment at CERN*. 2023. URL: https://home.cern/science/experiments/compass.

[7] CERN. *ATLAS experiment at CERN*. 2023. URL: https://home.cern/science/experiments/atlas.

[8] F. Sauli. "The gas electron multiplier (GEM): Operating principles and applications". In: *NIM A* 805 (2016), p. 3.

[9] R. Chechik, A. Breskin, C. Shalem, and D. Mörmann. "Thick GEM-like hole multipliers: properties and possible applications". In: *NIM A* 535 (2004), p. 303. ISSN: 0168-9002. URL: https://doi.org/10.1016/j.nima.2004.07.138.

[10] A. Breskin, R. Alon, M. Cortesi, R. Chechik, J. Miyamoto, V. Dangendorf, J. Maia, and J. [Santos]. "A concise review on THGEM detectors". In: *NIM A* 598 (2009). Instrumentation for Collding Beam Physics, p. 107. ISSN: 0168-9002. URL: http://www.sciencedirect.com/science/article/pii/S0168900208012047.

[11] A. Breskin, M. Cortesi, R. Alon, J. Miyamoto, V. Peskov, G. Bartesaghi, R. Chechik, V. Dangendorf, J. Maia, and J. [Santos]. “The THGEM: A thick robust gaseous electron multiplier for radiation detectors”. In: *NIM A* 623 (2010). 1st International Conference on Technology and Instrumentation in Particle Physics, p. 132. ISSN: 0168-9002. URL: `http://www.sciencedirect.com/science/article/pii/S0168900210004390`.

[12] A. Bondar, A. Buzulutskov, L. Shekhtman, and A. Vasiljev. “Study of ion feedback in multi-GEM structures”. In: *Nuclear Instruments and Methods in Physics Research Section A: Accelerators, Spectrometers, Detectors and Associated Equipment* 496.2 (2003), pp. 325–332. ISSN: 0168-9002. DOI: `https://doi.org/10.1016/S0168-9002(02)01763-1`. URL: `https://www.sciencedirect.com/science/article/pii/S0168900202017631`.

[13] A. B. Arons and M. B. Peppard. “Einstein’s Proposal of the Photon Concept—a Translation of the Annalen der Physik Paper of 1905”. In: *American Journal of Physics* 33.5 (May 1965), pp. 367–374. ISSN: 0002-9505. DOI: `10.1119/1.1971542`. eprint: `https://pubs.aip.org/aapt/ajp/article-pdf/33/5/367/12040128/367\_1\_online.pdf`. URL: `https://doi.org/10.1119/1.1971542`.

[14] W. R. Leo. *Techniques for nuclear and particle physics experiments: a how-to approach*. Springer Science & Business Media, 2012, p. 178.180.

[15] R. Chechik, A. Breskin, and C. Shalem. “Thick GEM-like multipliers—a simple solution for large area UV-RICH detectors”. In: *NIM A* 553 (2005). Proceedings of the fifth International Workshop on Ring Imaging Detectors, p. 35. ISSN: 0168-9002.

[16] M. Alexeev, R. Birsa, F. Bradamante, A. Bressan, M. Chiosso, P. Ciliberti, G. Croci, M. Colantoni, S. Dalla Torre, S. D. Pinto, O. Denisov, V. Diaz, A. Ferrero, M. Finger, M. Finger, H. Fischer, G. Giacomini, M. Giorgi, B. Gobbo, F. Heinsius, F. Herrmann, V. Jahodova, K. Königsmann, L. Lauser, S. Levorato, A. Maggiora, A. Martin, G. Menon, F. Nerling, D. Panzieri, G. Pesaro, J. Polak, E. Rocco, L. Ropeleswki, F. Sauli, G. Sbrizzai, P. Schiavon, C. Schill, S. Schopferer, M. Slunecka, F. Sozzi, L. Steiger, M. Sulc, S. Takekawa, F. Tessarotto, and H. Wollny. “THGEM based photon detector for Cherenkov imaging applications”. In: *Nuclear Instruments and Methods in Physics Research Section A: Accelerators, Spectrometers, Detectors and Associated Equipment* 617.1 (2010). 11th Pisa Meeting on Advanced Detectors, pp. 396–397. ISSN: 0168-9002. DOI: `https://doi.org/10.1016/j.nima.2009.08.087`. URL: `https://www.sciencedirect.com/science/article/pii/S0168900209017173`.

[17] J. Agarwala, M. Alexeev, C. D. R. Azevedo, F. Bradamante, A. Bressan, M. Buechele, C. Chatterjee, M. Chiosso, A. Cicuttin, P. Ciliberti, M. L. Crespo, S. D. Torre, S. Dasgupta, O. Denisov, M. Finger, M. F. J. au2, H. Fischer, M. Gregori, G. Hamar, F. Herrmann, S. Levorato, A. Martin, G. Menon, D. Panzieri, G. Sbrizzai, S. Schopferer, M. Slunecka, M. Sulc, F. Tessarotto, J. F. C. A. Veloso, and Y. Zhao. *The Hybrid MPGD-based photon detectors of COMPASS RICH-1*. 2018. arXiv: `1812.06971 [physics.ins-det]`.

[18] S. D. Pinto, M. Villa, M. Alfonsi, I. Brock, G. Croci, E. David, R. de Oliveira, L. Ropelewski, and M. van Stenis. "Progress on large area GEMs". In: *Journal of Instrumentation* 4.12 (2009), P12009.

[19] A. Utrobicic, M. Kovacic, F. Erhardt, N. Poljak, and M. Planinic. "A floating multi-channel picoammeter for micropattern gaseous detector current monitoring". In: *Nuclear Instruments and Methods in Physics Research Section A: Accelerators, Spectrometers, Detectors and Associated Equipment* 801 (2015), pp. 21–26. ISSN: 0168-9002. DOI: `https://doi.org/10.1016/j.nima.2015.08.021`. URL: `https://www.sciencedirect.com/science/article/pii/S0168900215009559`.

[20] B. Ulukutlu. *A search for new materials and the development of a readout system for particle detector applications*. 2021. URL: `https://www.das.ktas.ph.tum.de/DasDocs/Public/Master_Theses/MastersThesis_BerkinUlukutlu.pdf`.

[21] M. Rieder. *Characterizing CsI Coated THGEMs for Photon Detection*. 2022. URL: `https://www.das.ktas.ph.tum.de/DasDocs/Public/Bachelor_Theses/BachelorThesis_MarkusRieder.pdf`.

[22] L. Hofbauer. *Development of a Trigger System with a Cosmic Muon Tracker*. 2021. URL: `https://www.das.ktas.ph.tum.de/DasDocs/Public/Bachelor_Theses/BachelorThesis_LuisHofbauer_final.pdf`.

[23] T. Zhao, Y. Chen, S. Han, and J. Hersch. "A study of electron drift velocity in Ar-CO2 and Ar-CO2-CF4 gas mixtures". In: *Nuclear Instruments and Methods in Physics Research Section A: Accelerators, Spectrometers, Detectors and Associated Equipment* 340.3 (1994), pp. 485–490. ISSN: 0168-9002. DOI: `https://doi.org/10.1016/0168-9002(94)90129-5`. URL: `https://www.sciencedirect.com/science/article/pii/0168900294901295`.

[24] COMSOL. *COMSOL - Software for Multiphysics Simulation*. 2023. URL: `https://www.comsol.com/`.

[25] CERN. *Garfield++*. 2023. URL: `https://garfieldpp.web.cern.ch/garfieldpp/`.